EPSC2017

LSE1 abstracts

EPSC Abstracts
Vol. 11, EPSC2017-25-1, 2017
European Planetary Science Congress 2017

Crater monitoring through social media observations

I. Gialampoukidis, S. Vrochidis and I. Kompatsiaris
Centre for Research and Technology Hellas, Information Technologies Institute (CERTH-ITI), Thessaloniki, Greece
E-mail: {heliasgj, stefanos, ikom}@iti.gr

Abstract

Lunar craters have attracted the attention of not only scientists but also citizens. Modern high-resolution cameras with zoom capabilities allow citizens to capture and share pictures of the Moon in Social Media platforms, such as Twitter. We have collected 69 pictures of the Moon, from 01-01-2017 to 17-04-2017, that have been uploaded on Twitter and have been associated with the keyword *#crater*. The lunar pictures are indexed using SIFT descriptors and are then clustered using density-based approaches to group them into the automatically detected levels of zoom.

1. Introduction

The automatic detection and classification of lunar craters have been one of the most important challenges among lunar experts. Several approaches have been proposed [7] to detect or count craters, in order to assist and accelerate the classification of space images. Crater shapes are changing in time and their transition to a more complex morphology has been investigated [5]. Other approaches involve the extraction of visual descriptors that are based on the Hough transform for the detection and counting of craters [3]. Contrary to the use of lunar catalogues of optical images [6], we propose in this work the monitoring of crater activity through social media observations.

2. Methodology and Results

We crawled from the Twitter API[1] 69 pictures of the Moon, from 01-01-2017 to 17-04-2017, in response to the keyword *#crater*. In Table 1 we present the number of pictures per month and the daily coverage:

$$\text{Daily coverage} = \frac{\text{number of pictures per month}}{\text{number of days per month}} \quad (1)$$

From each crawled Twitter image, we extract salient points using the Lip-vireo[2] tool, in order to index all images using SIFT descriptors [4]. The Bag-of-Visual-Words representation is followed [2] using term frequency - inverse document frequency (tf-idf) scores, using a visual vocabulary of 100 visual words, obtained by k-means clustering with 30 iterations to ensure convergence in the visual vocabulary creation.

Table 1: Uploaded pictures per month.

Month	Pictures	Daily Coverage
January	23	74.19%
February	19	67.86%
March	16	51.61%
April (1st-17th)	11	64.70%

After the indexing of each image, an OPTICS reachability plot [1] is employed to visualize the cluster structure, i.e. the number of clusters and the optimal density level. The OPTICS reachability plot indicates that the dataset has two density-connected groups of pictures (clusters), which are extracted at the density level $\epsilon = 0.05$, while a lower bound for the number of pictures per cluster is $minPts = 5$. The adoption of a density-based clustering approach allows the presence of noise in the dataset and does not require a priori knowledge of the number of clusters. In Figure 1 we present a sample of the two detected groups of lunar images and one additional group of images (noise).

3. Summary and Conclusions

We have collected more than one image per two days, on average, in response to the keyword *#crater*. Each one of the collected images has been clustered into two main groups of images and an additional cluster is provided (noise) with pictures that have not been assigned to any cluster. The proposed lunar image

[1] https://dev.twitter.com

[2] http://pami.xmu.edu.cn/ wlzhao/lip-vireo.htm

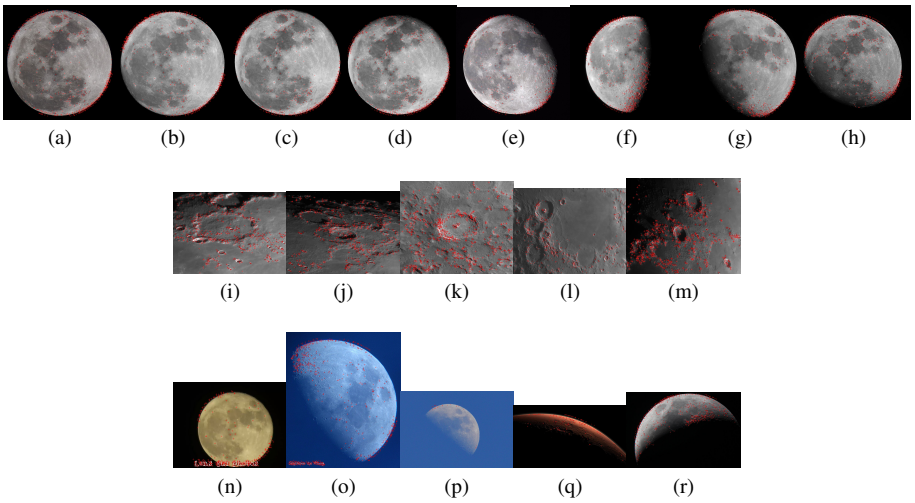

Figure 1: Sample of the pictures per group. The salient points that have been detected are shown on each image. The first group of pictures (a)-(h) shows a complete facet of the Moon, while the second group (i)-(m) zooms into craters. The last group (n)-(r) belongs to the set of unassigned pictures to any of the first two groups (noise).

clustering process provides two classes of lunar pictures, at different zoom levels; the first showing a clear view of craters grouped into one cluster and the second demonstrating a complete view of the Moon at various phases that are correlated with the crawling date. The clustering stage is unsupervised, so new topics can be detected on-the-fly. We have provided additional sources of planetary images using crowdsourcing information, which is associated with metadata such as time, text, location, links to other users and other related posts. This content has crater information that can be fused with other planetary data to enhance crater monitoring. The classification of each new Twitter picture is marked as relevant manually, but we plan to train a binary classifier for that purpose.

Acknowledgements

This work has supported by the EC-funded project KRISTINA (H2020-645012).

References

[1] Ankerst, M., Breunig, M. M., Kriegel, H. P., Sander, J.: OPTICS: ordering points to identify the clustering structure. In ACM SIGMOD record, Vol. 28, No. 2, pp. 49–60, 1999.

[2] Feng, J., Jiao, L. C., Zhang, X., Yang, D.: Bag-of-visual-words based on clonal selection algorithm for SAR image classification. IEEE Geoscience and Remote Sensing Letters, Vol. 8, No. 4, pp. 691–695, 2011.

[3] Galloway, M. J., Benedix, G. K., Bland, P. A., Paxman, J., Towner, M. C., Tan, T.: Automated crater detection and counting using the hough transform. In Image Processing (ICIP), 2014 IEEE International Conference on, pp. 1579–1583, 2014.

[4] Lowe, D. G.: Distinctive image features from scale-invariant keypoints.: International journal of computer vision Vol. 60, No. 2, pp. 91–110, 2004.

[5] Mahanti, P., Robinson, M., Povilaitis, R.: Crater shapes in transition – classification of lunar impact craters in the 5 km to 20 km size range, European Planetary Science Congress, 16–21 October, Pasadena, CA, USA, 2016.

[6] Salamunićcar, G., Lončarić, S., Grumpe, A., Wöhler, C.: Hybrid method for crater detection based on topography reconstruction from optical images and the new LU78287GT catalogue of Lunar impact craters. Advances in Space Research, Vol. 53, Vo. 12, pp. 1783–1797, 2014

[7] Sawabe, Y., Matsunaga, T., Rokugawa, S.: Automated detection and classification of lunar craters using multiple approaches. Advances in Space Research, Vol. 37, No. 1, pp. 21–27, 2006.

EPSC Abstracts
Vol. 11, EPSC2017-116, 2017
European Planetary Science Congress 2017

Investigation on the formation of lunar swirls based on Chang'E-1 IIM data

D. Liu (1, 2), W. Wen (1, 2), F. Wang (1, 2), X. Zhang (1, 2) and L. Geng (1, 2).
(1) National Astronomical Observatories, Chinese Academy of Sciences, Beijing, China, (2) Key Laboratory of Lunar and Deep Space Exploration, Chinese Academy of Sciences, Beijing, China.(liudw@nao.cas.cn)

Abstract

The formation of lunar swirls remains a mystery for many years. One leading hypothesis for the origin of lunar swirls was solar wind deflection model which explains its formation as the mass fraction difference of submicroscopic iron (SMFe) between on- and off-swirl regions. In this study, an empirical method was used to estimate mass fraction of SMFe of lunar swirls based on Change'E-1 IIM data. Results indicate that solar wind model is a validate hypothesis for the formation of lunar swirls.

1. Introduction

Lunar swirls are bright curvilinear marking on the lunar surface. They are optically immature than the surrounding areas and coincident with regions possessing high magnetic field strength, but not associated with distinct topography [1]. Elucidating the origin of lunar swirls is central to understanding the relative importance of solar wind implantation and micrometeorite bombardment on space weathering, and the origin of lunar surface magnetic field. One leading hypothesis for the formation of lunar swirls is solar wind deflection model. This model states that because of the deflection effect of lunar magnetic anomalies, a less amount of SMFe is generated in on-swirl regions due to a reduced solar wind flux, resulting in higher albedo of the lunar on-swirl regions than off-swirl regions to which solar wind ions are deflected to and a higher amount of SMFe is accumulated [2].

In this study, an empirical approach described in [3] was applied to estimate mass fraction of SMFe in on- and off- swirl regions using Chang'E-1 IIM data. We aimed to test whether on-swirl regions are indeed deficient in mass fraction of SMFe relative to off-swirl regions and whether solar wind deflection model is a valid hypothesis for the formation of lunar swirls.

2. Study Areas and Dataset

Three lunar swirls including Reiner Gamma, Firsov and a portion of Ingenii were investigated in this study. Their geological settings, magnetic field strength, and locations are shown in Table 1. Three sub-images of Chang'E-1IIM Level 2C radiance data were used in this study. They cover the central portion of these three swirl regions, and have been normalized to a standard geometry (i=g=30^o, e=0^o).

3. Method

Through conducting correlation analysis to the lunar soil samples from Lunar Soil Characterization Consortium (LSCC), Liu and Li (2015) [3] found that the ratio of 540 nm/810 nm single scattering albedo (SSA) of lunar soils is highly correlated with the mass fraction of SMFe. A simple exponential function can be used to describe this correlation as indicated in Fig.1. This exponential function was used in this work to estimate the mass fraction of SMFe in on- and off-swirl regions.

The radiance data of the three sub-images were first converted to reflectance by: R=(I/Istd)*Rstd, where Rstd is lab measured reflectance of lunar soil sample 62231, Istd is the corresponding radiance data of Apollo 16 landing site extracted from Chang'E-1 IIM 2C data, and I is the radiance data of sub-images covering the three swirl regions. Then, the reflectance data were converted to SSA using Hapke's radiative transfer model. The closest bands of Chang'E-1 IIM data to 540 nm and 810 nm used in the exponential function are 541 nm and 818 nm, respectively. However, 841 nm band of Chang'E-1 IIM data was selected rather than 818 nm band because of its high noise. At last, the ratio of 541 nm SSA/841 nm SSA was used in the exponential function to estimate the mass fraction of SMFe in Reiner Gamma, Firsov and Ingenii.

4. Results and Discussion

Shown in Fig. 2b is the mass fraction of SMFe of Ingenii. Off-swirl regions evidently possess higher mass fraction of SMFe than on-swirl regions. The derived mass fraction of SMFe ranges from 0% to 0.60% consistent with the measured data of lunar soils (0~0.5%) [4]. Similar trend was also found for swirl Reiner Gamma and Firsov.

Off-swirl regions are indeed enriched in SMFe as postulated by the solar wind deflection model. Because of the shielding effect of magnetic field, fewer solar wind ions, especially H^+ could penetrate into on-swirl regions and thus fewer Fe^{2+} could be reduced and sputtered to form SMFe. In contrast, implanted H^+ could be deflected onto off-swirl regions, resulting in higher amount of SMFe accumulated in off-swirl regions than in on-swirl regions.

5. Conclusions

Results from this work imply that solar wind deflection model is a validate hypothesis for the formation of lunar swirls. Moreover, this study indicates that solar wind ion implantation could be the major mechanism of space weathering rather than micrometeoroid impacts. Otherwise, the mass fraction difference of SMFe between on- and off-swirl regions would be absent.

References

[1] Blewett, D. T., et al.: Lunar swirls: Examining crustal magnetic anomalies and space weathering trends, J. Geophys. Res., 116, E02002, 2011.

[2] Hood, L. L. and Schubert, G.: Lunar magnetic anomalies and surface optical properties, Science, 08, 49–51, 1980.

[3] Liu, D. and Li, L.: An empirical approach to estimating mass fraction of submicroscopic iron in lunar soils, 46th Lunar and Planetary Science Conference, #2560, 2001.

[4] Morris, R.: Origins and size distribution of metallic iron particles in the lunar regolith, Proc. Lunar Sci. Conf. 11, 1697-1712, 1980.

Table 1: Lunar swirls investigated in this study

Swirls	Locations	Geological Setting	Magnetic Anomaly Strength (nT)
Reiner Gamma	7.5ºN, 302.5ºE	Mare	22 - Strong
Firsov	10.5ºS, 16.5ºE	Highland	11- Moderate
Ingenii	33.5ºS, 160ºE	Highland	20 - Strong

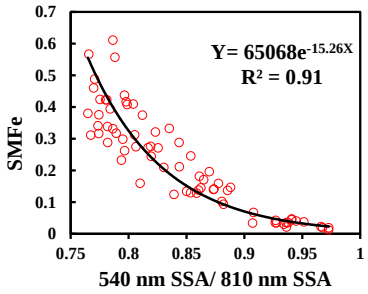

Figure 1: Correlation between the ratio of 540 nm SSA/810 nm SSA and SMFe for LSCC soil samples

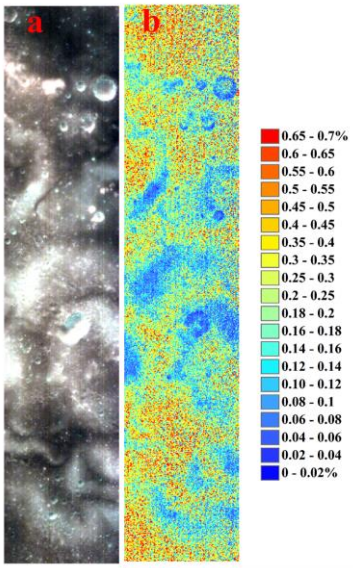

Figure 2: (a) Chang'E-1 IIM false color composite (R = 865 nm, G = 645 nm, B = 550 nm) for a portion of Ingenii. (b) Mass fraction of SMFe.

EPSC Abstracts
Vol. 11, EPSC2017-212-2, 2017
European Planetary Science Congress 2017

Science case for Ultra-Long-Wavelength Astronomy from the Moon's surface and vicinity

L.I. Gurvits (1,2)

(1) Joint Institute for VLBI ERIC, Dwingeloo, The Netherlands (lgurvits@jive.eu)
(2) Department of Astrodynamics and Space Missions, Delft University of Technology, Delft, The Netherlands

The Ultra-Long-Wavelength (ULW) range of the electromagnetic spectrum (wavelengths longer than ~15 m, frequencies below ~20 MHz) is the last unexplored window into the electromagnetic Universe. At this wavelength regime, the Earth's ionosphere does not allow the cosmic electromagnetic emission to reach the Earth's surface. Thus, observations of celestial sources in this spectrum domain are possible only from space-borne radio telescopes.

The ULW range is offering unique opportunities for pioneering research in many fields of astrophysics and cosmology, from Solar-terrestrial studies, to Galactic and extragalactic radio astronomy (Jester and Falcke 2009 and references therein). Particularly attractive are applications of ULW observations for studies of Fast Radio Bursts (FRB), pulsars, and imprints of the cosmological evolution of the Universe in the distribution of highly redshifted emission of the atomic hydrogen (HI). Studies of cosmic radio emission in the ULW regime are also very informative for diagnostics of the interplanetary plasma and properties of the planetary bodies in the Solar system.

From the technological perspective, the ULW instrumentation is relatively simple and affordable. It can be based on the widely available instrumentation, developed for the Earth-based radio astronomy of shorter wavelengths (meters and shorter). An issue of special concern for ULW astronomy is protection from and mitigation of human-made radio frequency interference (RFI) that can affect operations of a radio telescope anywhere in the Earth's vicinity up to distances of tens of the Earth diameters and even farther away. The Moon represents a natural and efficient shield from the Earth-originated RFI.

An ULW astronomical facility can be placed on a free-flying platform on a selenocentric orbit, e.g. as described by Boonstra et al. 2016, or on the Moon far side (Mimoun et al. 2014). The latter case is especially attractive with the ULW radio telescope permanently shielded from the Earth-originated RFI. Economically attractive might be an option of placing an ULW radio telescope near the southern pole of the Moon with the crater rim offering sufficiently efficient protection from the Erath-originated RFI.

An ULW facility of the first generation does not require for its operations significant power and extensive maintenance, its mass is measured in kilograms, not tons. It is perfectly suitable for the role of a cost-efficient "piggy-back" payload for the early wave of Moon exploration missions.

References

Boonstra A.-J. et al. 2016, *"Discovering the sky at the Longest Wavelengths (DSL)"*, IEEE Conference Publications, DOI: 10.1109/AERO.2016.7500678

Jester S., and Falcke H. 2009, *"Science with a lunar low-frequency array: from the dark ages of the Universe to nearby exoplanets"*, New Astronomy Review, 53, 1–26

Mimoun D. et al. 2012, "*Farside explorer: unique science from a mission to the farside of the Moon*", Experimental Astronomy, 33(2-3), 529–585

EPSC Abstracts
Vol. 11, EPSC2017-235, 2017
European Planetary Science Congress 2017

Magnetization Distribution for the Schlüter P. Lunar Magnetic Anomaly

D. Constantinescu (1,2), K.H. Glassmeier (2), U. Auster (2), D. Frühauff (2), F. Plaschke (3)
(1) Institute for Space Sciences, Bucharest, Romania (d.constantinescu@tu-bs.de)
(2) Institute for Geophysics and Extraterrestrial Physics, TU Braunschweig, Germany
(3) Space Research Institute, Austrian Academy of Sciences, Graz, Austria

Abstract

Using magnetic field data measured during three low altitude passes of the ARTEMIS P1 probe over the same region of the Moon, we are able to identify and characterize a weak magnetic anomaly in the vicinity of the Schlüter P. crater. The measurements are done in quiet solar wind conditions on the night side of the Moon while the second ARTEMIS spacecraft is used to simultaneously monitor the variations of the interplanetary magnetic field. The measured magnetic field is then compared with the terrain elevation from Lunar Reconnaissance Orbiter and with the gravitational field derived from the GRAIL spacecraft observations. We find that the magnetic field variations show a dependence on the terrain elevation and also on both the free air and the Bouger gravitational anomalies. This indicates that the surface magnetization follows the terrain and that the layer just below the terrain is characterized by patchy magnetization closely related with the density variations.

1. Introduction

Even though the first measurements of the lunar crust magnetization were done in the Apollo era [11, 6] and in the last two decades high resolution mapping of the lunar surface field was realised based on Lunar Prospector [4] and Kaguya [8] data [12, 9], the relation between the lunar crust magnetization and the surface features remained elusive. The concentration of strong magnetic anomalies at the antipodes of large impact basins [7] can be explained by compression of the pre-existing ambient magnetic field by the plasma cloud created by the impact converging towards the antipode. The impact basins themselves exhibit low magnetization, as do in general the smaller impact craters too [12].

Comparing crustal magnetization models with the Lunar Prospector data shows that the magnetized sources in the lunar crust can be represented by a magnetized layer with the thickness of about 30 km and average magnetization of 30-40 mA/m [5]. The distribution of the magnetized material within this layer is less known. On one hand, large scale magnetic anomalies, observable from the orbit, require the presence of strong coherent remnant magnetization sources. On the other hand, fields measured by the Apollo surface magnetometers have shown a great variety in strength and orientation on km scales, suggesting localized sources close to the surface [6]. We show that - for the Schlüter P. magnetic anomaly - there is a correlation between the elevation of the Moon's surface and the magnetic field measured on orbit. This proves that the near-surface magnetization contributes to the large scale magnetic anomaly. We also show that deeper magnetized sources, associated with density variations bring a comparable contribution to the Schlüter P. magnetic anomaly.

2. Data

After the initial phase of the THEMIS mission [1] was completed in 2009, two of the five spacecraft were sent to the Moon to form the ARTEMIS mission [2]. In this work we use magnetic field data measured by the FGM instrument [3] onboard these probes. Due to their highly elliptical equatorial orbits, the low altitude segments of the orbits were grouped only in four areas in the equatorial region. Up to now, we counted only 47 orbits having a periselene lower than 45 km AGL. To be able to separate the magnetic field originating from the crust from external fluctuations, we select only the intervals when the Moon was in the pristine solar wind and the measurements were done on the night side. This leaves us with only 16 orbit segments. Three of them, illustrated in Fig. 1 show high correlation between the measured magnetic fields.

The Lunar Reconnaissance Orbiter Camera [10] data obtained from the NASA Planetary Data System

(PDS) was used for the surface elevation. The lunar gravitational field data, also obtained from PDS, was delivered by the Gravity Recovery and Interior Laboratory (GRAIL) mission [13]

3. Schlüter P. magnetic anomaly

In the vicinity of the Schlüter P. crater, located on the equator, north of Mare Orientale we identified a weak magnetic anomaly revealed by the correlation between the measured magnetic field along three orbit segments with the closest approach of 12, 20, and 29 km AGL, respectively. The maximum peak to peak variations of the measured magnetic field were in the order of 4 nT. From measurements at different altitudes, if we assume a cubic decay of the field intensity, we can associate the strongest field variation with an equivalent dipole buried 13 km below the surface and producing a surface field of about 36 nT. The magnetization corresponding to a magnetized sphere centred on the dipole and touching the surface would be about 80 mA/m.

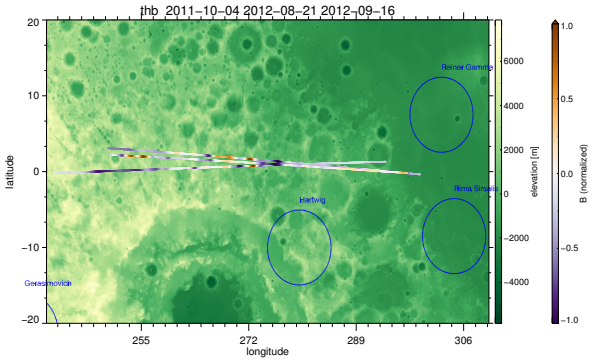

Figure 1: ARTEMIS orbit segments below 100 km over the Schlüter P. magnetic anomaly. The background image shows the terrain elevation from LRO data, The orbit colour represents the measured magnetic field, and the blue markings show known magnetic anomalies

4. Magnetization distribution

One way to obtain information on the distribution of the magnetized material below the lunar surface is to establish if there is a relation between the magnetic field measured on orbit and variations in the terrain elevation and in the lunar gravitational field. This can be done by analysing the phase difference between the measured magnetic field and the quantities named above. We obtained the time and frequency dependent phase shift from the cross-spectrum between the magnetic field and the elevation and gravitational field variations, respectively. We found that, far from being random as expected for un-related quantities, the phase shift was consistently close to the same value for the three tested orbit segments for all relevant frequencies. This holds true for the elevation, free air and Bouger gravitational anomalies.

By comparing our results with possible combinations of uniform and patchy distributions of the subsurface magnetized material and density, we are able to show that near-surface magnetization has a significant contribution to the overall magnetic anomaly. At the same time, magnetized sources correlated with density variations in deeper layers generate much of the magnetic anomaly field.

5. Summary and Conclusions

A new magnetic anomaly close to the Schlüter P. lunar crater was identified from ARTEMIS magnetic field data. The anomaly is rather weak, with surface fields in the order of 30 nT.

The magnetic field variations are correlated with the terrain elevation, with the free air gravitational anomaly, and with the Bouger gravitational anomaly.

The sources of the Schlüter P. magnetic anomaly are distributed both near the lunar surface, following the terrain, and in the depth, where the magnetization is closely related with the crust density variations.

References

[1] Angelopoulos, V. *Space Sci Rev*, pp. 47–+, 2008

[2] Angelopoulos, V. *Space Sci Rev*, pp. 114–137, 2010

[3] Auster, H. U., et al. *Space Sci Rev*, pp. 73–+, 2008

[4] Binder, A. B. *Science*, 281:1475, 1998

[5] Carley, R. A., et al. *JGR Plan*, 117(E8), 2012. E08001

[6] Dyal, P., et al. *Science*, 169:762, 1970

[7] Hood, L. L. and Vickery, A. In *Lunar Plan. Sci. Conf. Proc.*, vol. 15, pp. C211–C223. 1984

[8] Kato, M., et al. *Space Sci Rev*, 154:3, 2010

[9] Richmond, N. C. and Hood, L. L. *JGR Plan*, 113:E02010, 2008

[10] Robinson, M. S., et al. *Space Sci Rev*, pp. 81–124, 2010

[11] Runcorn, S. K., et al. *Geochimica et Cosmochimica Acta Supplement*, 1:2369, 1970

[12] Tsunakawa, H., et al. *JGR Plan*, 120:1160, 2015

[13] Zuber, M. T., et al. *Space Sci Rev*, pp. 3–24, 2013

EPSC Abstracts
Vol. 11, EPSC2017-276-2, 2017
European Planetary Science Congress 2017

The observation and coverage analysis of the moon-based ultraviolet telescope on CE-3 lander

Wang,F.,Wen,W.-B., Liu, D.-W.,Geng, L., Zhang X.-X., Zhao,S.
Key Laboratory of Lunar and Deep Space Exploration,Chinese Academy of Sciences；National Astronomical Observatories,Chinese Academy of Sciences，Beijing, China (wangf@bao.ac.cn / Fax: +86-010-64888703)

Abstract

The moon-based ultraviolet telescope (MUVT) is one of the payloads on CE-3 lunar lander. This article presents the statistics and analysis of observation coverage during the period of MUVT working from December 15, 2013 to December 2, 2015, a total of 25 months. The results show that MUVT implemented about 5.487% of a total survey area, to achieve the CE-3 survey mission. It has accumulated lots of observational data for research on stellar evolution, compact star and so on.

1. Introduction

In accordance with CE-3 mission, taking the Moon as a natural astronomical observation platform, MUVT works in the near ultraviolet spectrum, it will be the first long-term observatory to be deployed on the Moon, to study on the variation characteristics of celestial bodies and sky survey of low galactic latitude.

The MUVT consists of a Ritchey-Chretien telescope(RCT) that is a specialized Cassegrain Telescope. It uses a pointing mirror that features a two-dimensional gimbal to track objects.

The CE-3 MUVT observation mode has two types: one is the pointing observation of astronomical sources for a long time; another is survey of low galactic latitude area by the rotation of the moon. At the same time, in order to ensure the validity of the astronomical observation data, the CE-3 MUVT has been working, including attitude calibration, and photometric calibration, the instrument correction.

2. Data processing and coverage analysis

We make a systematic analysis and evaluation of the data acquisition, processing and survey of the MUVT from December 15, 2013 to December 2, 2015. For the MUVT, data processing includes: firstly, frame synchronization, decoding, sorting, and data decompression, secondly, physical transformation of data blocks, finally the data for instrument effect correction, background removal and positioning in celestial coordinate system.

The celestial coordinates in J2000 mean equatorial coordinate system are calculated for the center and the four corners for each of the images. The calculation is based on the pitch and azimuth angles of the gimbal and on the relationship between the attitude of the telescope and the lunar rotation pole.

In order to maintain the survey path of the MUVT and the shape of each image, and reduce the angular distortion of the image, when the data analysis and statistics, we use the azimuthal projection (the center of the projection is Latitude 65 degrees , Longtitude -90 degree).

Due to the limit of pitch angle between +11degreee ~+20 degree(zenith 0, north is positive), the north latitude 60 degree is within the observation range. According to the point observation, survey and attitude calibration three types, we perform our coverage analysis through the time stamp and coordinates of the MUVT images.

3. Figures

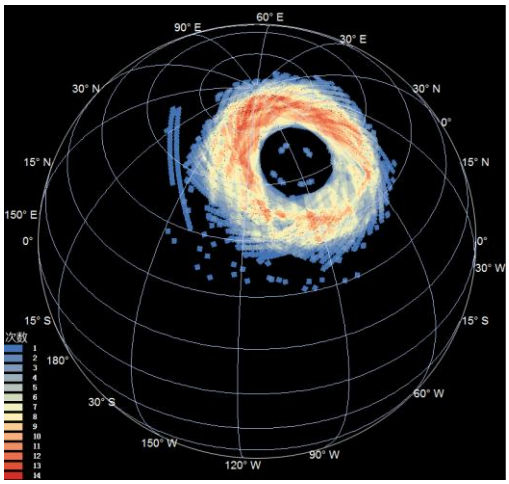

Figure 1: the coverage analysis results of MUVT during two years.

6. Summary and Conclusions

Through the analysis of all the observed images of MUVT, it is found that in the celestial coordinate system, all the images of the survey are concentrated at Latitude 65 degrees and Longtitude -90 degrees as the center, a ring of 15 degrees width. The observation data analysis: the coverage of the northern area is up to 2263.8 square degrees, accounting for about 5.487% of the all area. The task is completed the observation target. For the first time, the MUVT in a long time has carried out the astronomical observations, and accumulated abundant observational data for basic research on the evolution of stars, compact star and high energy astrophysics and so on.

Acknowledgements

We wish to thank all members from the Ground Research and Application System and the Moon-based Ultraviolet Telescope instrument group(Key Laboratory of Space Astronomy and Technology) that is part of the Chang'e-3 program, whose joint efforts have made the data acquisition and preprocessing used for this study possible.

References

[1] Wen W. B., Wang F.， et al. Data preprocessing and preliminary results of the moon-based ultraviolet telescope (MUVT) on CE-3 detector.RAA,2014.

[2]Tan X., Liu J. J., Li C. L., et al. 2014, Research in Astron. Astron. Astrophys. (RAA), 2014.

[3] Jia Yingzhuo. The report of the CE3' payload flight model, 2011.

[4] Cao Li. The calibration summary report of the moon ultraviolet telescope, one of the CE-3' payloads. 2012.

[5] J. Wang, J. S. Deng, J. Cui et: Lunar exosphere influence on lunar-based near-ultraviolet astronomical observations, 2011 (In Adv. Space Res.).

[6]Ip,W.-H.,Yan,J.,Li,C.-L.,&Ouyang,Z.-Y.,2014,RAA(Research in Astronomy and Astrophysics),14,1511

EPSC Abstracts
Vol. 11, EPSC2017-290, 2017
European Planetary Science Congress 2017

Detection of Lunar Lava Tubes with Orbiting Radar Sounder Systems

L. Carrer, C. Gerekos and L. Bruzzone
Department of Information Engineering and Computer Science, University of Trento, Italy.

Abstract

Lunar lava tubes are subsurface structures which are potential candidates for future human outposts on the Moon. Recently, remote sensing observations of the Moon based on optical cameras and gravitational field mapping have detected features which can be directly related to the presence of lava tubes. However, the potential for global lava tubes mapping using these types of sensors is very limited. In order to accurately detect lava tubes it is necessary to perform direct subsurface measurements of the shallow lunar subsurface. This can be done by radar sounders which are electromagnetic instruments specifically designed to detect and classify subsurface features from orbit. However, past Moon radar sounder missions were not aiming for for lava tubes exploration, and had thus limited capability to detect them. In this paper, we have studied the optimal type of orbiting radar instrument that would be needed to detect the majority of lunar lava tubes, based on their expected properties. To define this instrument, we conducted both a performance assessment versus different parameters of the radar sounder and an electromagnetic signature analysis to determine the possibility to detect lava tubes having different sizes from orbit.

1. Introduction

Lunar lava tubes are considered to be one of the main candidates for future human outposts [1] as they can offer shelter against meteorite impacts, radiation, and strong thermal variations taking place on the Moon surface. They are natural subsurface conduits which are the result of past volcanic activity. Recent studies based on gravity measurements [2] and experimental evidence based on terrain mapping cameras [3] suggest that there is an abundance of lava tubes scattered across the Moon. However, lava tube mapping with an optical camera has limitations due to the fact that they are essentially subsurface structures. In this context, spaceborne radar sounder instruments are particularly suitable for revealing the presence of lava tubes due to their ability to remotely probe the subsurface of a planetary body. By analyzing the electromagnetic characteristic of the echo signals received by a radar optimized for lava tube detection we expect that it is possible to infer the physical composition of a lava tube, its size and shape as well as the nature of the material forming the lava tube roof and floor.
Very recently, researchers detected in the data acquired by the Lunar Radar Sounder (LRS) an intact lava tube [4]. On the one hand this confirms the capability of sounders to detect lava tubes. On the other hand, LRS has not been specifically designed for the detection of lava tubes. Thus, due to its very low carrier frequency (and thus spatial resolution), it can only detect very large lava tubes. Accordingly, the detection of small and shallower lava tubes appears to be very unlikely with LRS. Moreover, shallow lava tubes are of high importance since it is easier to explore them either by manned and unmanned missions.
In this paper we present a study for the design of an orbital radar sounder optimized for detecting lunar lava tubes of various dimensions. This is done by providing a detailed perfomance analysis versus different radar parameters. Our analysis is complemented by extensive simulations of the lunar lava tubes electromagnetic responses by means of a 3D coherent multilayer radar echo simulator. In our study, the allowed lava tube sizes in terms of roof height and width are those provided in the recently published structural stability analysis by Blair et al. [2]. Accordingly, structurally unstable lava tubes have not been considered in our analysis.

2. Radar Sounder for Lava Tubes Detection

The study on a radar sounder for lava tubes detection was performed considering realistic parameters such as the ones on orbital configuration of the spacecraft and transmitted power by taking into account the heritage of previous radar sounding missions. Regarding the surface and subsurface parameters, we assumed a representative yet challenging scenario which implies a large radar signal attenuation. To this extent, we considered a regolith mantling layer covering the lava tube roof of variable thickness and consisting of basaltic material. The lava tube floor is considered basaltic as well. The analyses on Signal to Noise Ratio (SNR) and Signal to Clutter Ratio (SCR) highlight that the main driving factor affecting the radar performance is the attenuation of the radar signal for fixed subsurface properties in terms of complex dielectric constant. It mainly depends on the lava tube roof height and on the radar central frequency. The capability to detect lava tubes with thin roof improves as the radar central frequency increases due to larger achievable radiated pulse bandwidth resulting in improved range resolution. The same behavior is found for the detection of lava tubes with small widths as horizontal resolution improves by increasing the central frequency. The detection of lava tubes having large roofs degrades as the central frequency increases due to attenuation in

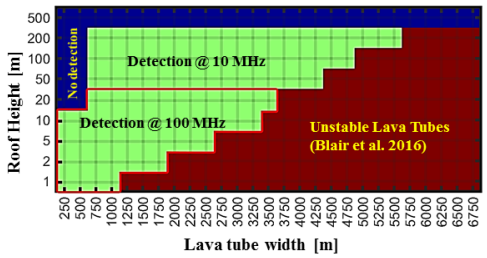

Figure 1: Detectable lava tubes matrix with dual carrier frequency sounding (10 MHz and 100 MHz).

the medium. By combining all these observations, we are naturally led to the conclusion that a radar sounder operating with a low central frequency (e.g. 10 MHz to 20 MHz) is suitable for detecting large lava tubes while a system with higher frequency (e.g. 80 MHz to 100 MHz) is suitable for detect small ones. Consequently, a multi-frequency radar sounder is needed to map the vast majority of stable lava tubes in terms of dimensions, as shown in the example of Fig. 1. The detection matrix is displayed in the same fashion as the structural stability one presented in [2].

3. Electromagnetic Signatures of Lava Tubes

We have analyzed the radar returns for different lava tubes geometries using a coherent 3D simulator we developed. The simulations were performed for different radar system parameters and for different crossing angles of the sensor over the investigated scene. Four representative lava tubes were selected, with dimensions based on the stability analysis of [2]: $w = 4000\,\text{m}$, $h = 200\,\text{m}$; $w = 3000\,\text{m}$, $h = 10\,\text{m}$; $w = 1250\,\text{m}$, $h = 50\,\text{m}$; and $w = 250\,\text{m}$, $h = 1\,\text{m}$, where w represents the lava tube width and h the roof depth. Simulations the surface terrain and the target lava tube were carried out at two different central frequencies, 10 MHz and 100 MHz. The bandwidth was set equal to half the central frequency in both cases. Procedurally generated fractional brownian motion surfaces were used to reproduce the lunar surface topography and subsurface roughness.

The electromagnetic simulations confirmed the conclusions of the performance analysis and were able to provide realistic examples of lava tube electromagnetic signatures acquired from lunar orbit with a dedicated radar sounder system. Electromagnetic signatures of small lava tubes are generally made of two vertically-aligned hyperbola sections, one for the lava tube roof and one for the lava tube floor. Large lava tubes show thicker and more linear contributions when compared to small ones (see Fig. 2) due to the wider scattering area.

Because of the relatively strong attenuation in the material composing the lava tube roof, the deeper lava tubes were only visible by the lower frequency

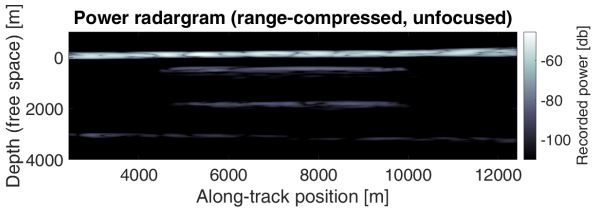

Figure 2: Example of simulated signature for a Moon lava tube with a width of 4 km and a roof height of 200 m as seen by a radar with a central frequency of 10 MHz and a bandwidth of 5 MHz. The sensor crossing direction is perpendicular to the lava tube axis. The fBm surface parameters are $H = 0.75$ and $T = 355\,\text{m}$.

radar. On the other hand, the upper hyperbola of the shallower lava tubes could be unambiguously distinguished from the surface return only with the high-frequency radar. The difference in signal intensity between the returns from lava tube roof and floor was never more than a few dBs in all cases, as it is only due to geometrical effects (there is no attenuation in the lava tube cavity).

4. Summary and Conclusions

Recent evidence based on optical camera surveys and gravity measurements suggest that there is a considerable number of lava tubes concealed under the surface of the Moon. In this paper we investigated the feasibility of detecting them from orbit with a radar sounder specifically designed for this task. To this extent, our performance analysis shows that a multi-frequency sounding system is the best option for detecting lava tubes of very different dimensions. The electromagnetic simulations show that lava tubes have unique electromagnetic signatures, which can be detected from various crossing configurations of the sensor when orbiting over the lava tube.

References

[1] F. Horz. Lava tubes - Potential shelters for habitats. In W. W. Mendell, editor, *Lunar Bases and Space Activities of the 21st Century*, pages 405–412, 1985.

[2] David M. Blair, Loic Chappaz, Rohan Sood, Colleen Milbury, Antonio Bobet, H. Jay Melosh, Kathleen C. Howell, and Andrew M. Freed. The structural stability of lunar lava tubes. *Icarus*, 282:47 – 55, 2017.

[3] AS Arya, RP Rajasekhar, Guneshwar Thangjam, Ajai Kumara, and AS Kiran Kumara. Detection of potential site for future human habitability on the moon using chandrayaan-1 data. *Current Science (00113891)*, 100(4), 2011.

[4] J Haruyama, T Kaku, R Shinoda, W Miyake, A Kumamoto, K Ishiyama, T Nishibori, K Yamamoto, K Kurosawa, AI Suzuki, et al. Detection of lunar lava tubes by lunar radar sounder onboard selene (kaguya). In *Lunar and Planetary Science Conference*, volume 48, 2017.

EPSC Abstracts
Vol. 11, EPSC2017-362, 2017
European Planetary Science Congress 2017

Imaging analysis of Kaguya Lunar Radar Sounder off nadir echo data

T. Kobayashi and S. R. Lee
Korea Institute of Geoscience and Mineral Resources, Daejeon, KOREA (tak@kigam.re.kr)

Abstract

We attempted surface imaging of the Moon using the off nadir echo data of Kaguya Lunar Radar Sounder (LRS). The primary purpose of this attempt is to detect very shallow subsurface signal of geologic structure such as lava tube which would not be discerned in nadir echo analysis due to poor range resolution of the LRS. The LRS range-echo data was mapped (projected) to the lunar surface, considering the lunar surface terrain elevation, to produce a mosaic image of the Moon. Multiple orbit data allows us to resolve the mirror image problem (one cannot discern which side of the orbit the received echo comes from because of the axisymmetric radiation pattern of a dipole antenna). Produced image is carefully checked in comparison with optical surface images. Preliminary analysis proved that LRS can image surface features such as craters, ridge systems and rilles.

1. Introduction

Kaguya LRS is an HF (5 MHz) radar sounder which flew to the Moon to explore subsurface geologic structure [3]. LRS successfully found layering structures in maria but the area where subsurface layering was found was rather limited. In addition, the apparent depth range of the layering structure was limited only to ~1000 meters at the maximum. The rest of LRS data in farther ranges was regarded as off nadir surface echoes. However, the "surface" echo of an HF radar such as LRS and MARSIS contains information of shallow subsurface (near surface) medium [1] [2], which is true not only to nadir echoes but also to off nadir echoes. This fact motivated us to make an attempt to extract subsurface information from off nadir echoes of LRS observation. In this study, we mapped (projected) LRS off nadir echoes to the lunar surface to make mosaic images of off nadir lunar surface, and, by doing so, we pursue shallow subsurface geologic structure.

2. Data mapping (projection)

Provided the nadir surface range being as the reference range, the LRS data in the range of 1000 m to 7000 m was mapped (projected) to the lunar surface which was defined by Kaguya Digital Terrain Model data [4]. Consideration of surface terrain elevation prevent the image from suffering "layover" problem. Gain control was applied so that the echo intensity variation as a function of range is flattened thus the detail feature of produced mosaic image is better recognized at visual inspections. Direction of LRS illumination, i.e. westward/eastward, was considered when the data was projected, and, as results, two images are produced for each imaged area. They should provide useful information concerning surface and shallow subsurface features when the image is interpreted

3. Preliminary result – Aristarchus plateau

Figure 1. shows the LRS projection images of Aristarchus plateau with a Kaguya Terrain Camera (TC) image as the reference. Aristarchus crater and neighboring Herodotus as well as Vallis Schröteri are well recognized in both westward illumination image and the eastward illumination image. Other rille systems and minor craters are also recognized but appears less prominent than major features. It should be noted that those features appear differently depending on the illumination direction of LRS. An interesting observation is that the plateau appears a little darker than surrounding mare plane, which suggests that the plateau surface is less rough in term of the LRS wave length scale (60 m) than surrounding mare surface.

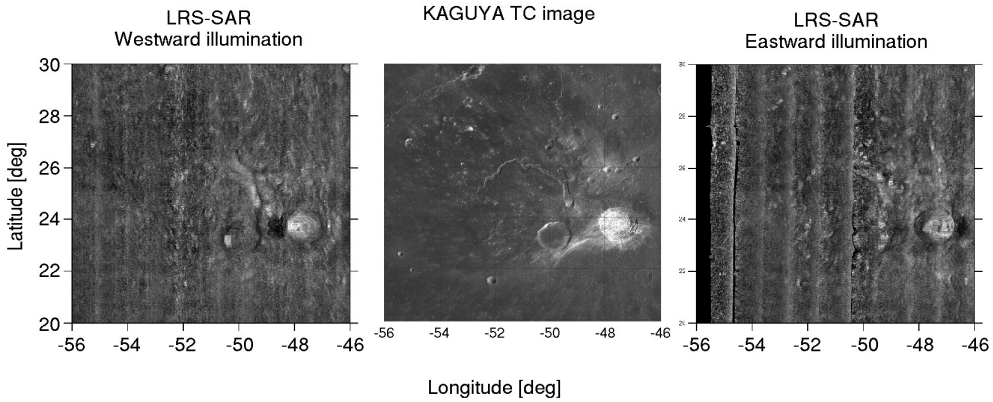

Fig. 1 Aristarchus plateau: LRS projection image of westward illumination (left), Kaguya TC image (center), and LRS projection image of eastward illumination (right).

4. Summary and Conclusions

We have established a procedure of LRS range-echo data mapping (projection) onto the lunar surface. The procedure takes into account the surface terrain elevation based on Kaguya DTM data. Global mapping (projection) work is currently in progress. Establishing a simulation procedure of LRS observation is also in progress so that suspicious features found in the LRS image is examined by simulations. The simulation is designed based on Kirchhoff approximation theory and Kaguya DTM is incorporated.

Acknowledgements

This work is supported by the research program KIGAM (17-3111) of Korea Institute of Geoscience and Mineral Resources.

References

[1] Kobayashi, T. et al.: Simultaneous observation of Lunar Radar Sounder and Laser Altimeter of Kaguya for lunar regolith layer thickness estimate, IEEE GRSL, Vol. 7, pp.435 – 439, 2010.

[2] Mouginot, J. et al.: MARSIS surface reflectivity of the south residual cap of Mars, Icarus, Vol. 201, pp.454 – 459, 2009.

[3] Ono, T. et al.: Lunar Radar Sounder observation of subsurface layers under the nearside maria of the Moon, Science, Vol. 323, pp.909 – 912, 2009.

[4] SELENE Data Archive, JAXA, http://l2db.selene.darts.isas.jaxa.jp/

EPSC Abstracts
Vol. 11, EPSC2017-480, 2017
European Planetary Science Congress 2017

Mini-RF bistatic observations of Copernican crater ejecta on the Moon

A.M. Stickle, G.W. Patterson, J.T.S Cahill, and the Mini-RF Team
Johns Hopkins Applied Physics Laboratory, 11100 Johns Hopkins Rd., Laurel, MD, USA 20723, (angela.stickle@jhuapl.edu/ Fax: +1-240-228-8939)

Abstract

The Mini-RF radar is current operating in a bistatic configuration using the Goldstone DSS-13 and Arecibo Observatory as transmitters in X-band (4.2-cm) and S-band (12.6 cm), respectively. A typical product examining the scattering properties of the lunar surface that can be derived from backscattered microwave radiation is the Circular Polarization Ratio (CPR). Here, we examine the ejecta blankets of Copernican aged craters on the lunar surface in both S- and X-band to examine the scattering properties of young crater ejecta. Several observed craters exhibit a clear opposition effect at low bistatic (phase) angles. This opposition effect is consistent with optical studies of lunar soils done in the laboratory, but these observations are the first time this effect has been measured on the Moon at radar wavelengths. Differences in the CPR behaviour as a function of bistatic angle may also provide opportunities for relative age dating between Copernican craters.

1. Introduction

The Mini-RF instrument aboard NASA's Lunar Reconnaissance Orbiter (LRO) is currently acquiring bistatic radar data of the lunar surface at both S-band (12.6 cm) and X-band (4.2 cm) wavelengths in an effort to understand the scattering properties of lunar terrains as a function of phase angle. Previous work, at optical wavelengths, has demonstrated that the material properties of lunar regolith can be sensitive to variations in phase angle [1-3]. This sensitivity gives rise to the lunar opposition effect and likely involves contributions from shadow hiding at low phase angles and coherent backscatter near zero phase [1]. Mini-RF bistatic data of lunar materials indicate that such behavior can also be observed for lunar materials at the wavelength scale of an S-band radar (12.6 cm). The ejecta blankets of seven lunar craters have been observed to date, and the Circular Polarization Ratio (CPR) examined as a function of

1.1 Bistatic Observation Campaign

Radar observations of planetary surfaces provide important information on the structure (i.e., roughness) and dielectric properties of surface and buried materials [4-7]. These data can be acquired using a monostatic architecture, where a single antenna serves as the signal transmitter and receiver, or they can be acquired using a bistatic architecture, where a signal is transmitted from one location and received at another. The former provides information on the scattering properties of a target surface at zero phase. The latter provides the same information but over a variety of phase angles. NASA's Mini-RF instrument on the Lunar Reconnaissance Orbiter is currently operating in a bistatic architecture with the Arecibo Observatory in Puerto Rico and the Goldstone DSS-13 antenna in California. The Arecibo Observatory serves as the transmitter for S-band operations and DSS-13 serves as the transmitter for X-band operations. In both cases and Mini-RF serves as the receiver. This architecture maintains the hybrid dual-polarimetric nature of the Mini-RF instrument [8] and, therefore, allows for the calculation of the Stokes parameters (S_1, S_2, S_3, S_4) that characterize the backscattered signal (and the products derived from those parameters).

2. Observations

A common product derived from the Stokes parameters is the Circular Polarization Ratio (CPR),

$$\mu_C = \frac{(S_1 - S_4)}{(S_1 + S_4)} \quad (1).$$

CPR information is commonly used in analyses of planetary radar data [4-7], and is a representation of surface roughness at the wavelength scale of the radar (i.e., surfaces that are smoother at the wavelength scale will have lower CPR values and surfaces that are rougher will have higher CPR

values). High CPR values can also serve as an indicator of the presence of water ice [9].

As part of the Mini-RF bistatic observation campaign, CPR information for a variety lunar terrains is being collected over a range of bistatic and incidence angles. The first campaign (during LRO extended mission targeted a variety of Copernican-aged impact craters in order to characterize the opposition response of materials known to be rough at radar wavelengths [10]. Patterson et al. [10] showed the ejecta properties for three of these craters: Byrgius A, Kepler, and Bouguer, as a function of bistatic angle. Both Kepler and Bygius A exhibited an opposition effect, while Bouguer did not. The opposition responses of Byrgius A and Kepler ejecta lead to increases in CPR of ~30% and 15%, respectively, as bistatic angle approaches 0°. The mean CPR of Byrgius A and Kepler ejecta at bistatic angles outside of their opposition responses averages ~20% higher than surrounding materials. The mean CPR of Bouguer averages ~5% above surrounding materials. Patterson et al. [10] suggest that the radar scattering characteristics of the continuous ejecta for these three craters, coupled with age estimates based on crater statistics and geologic mapping, suggest a relationship between the opposition response of the ejecta and the age of the crater (i.e., Byrgius A is the youngest of the craters observed and shows the strongest response). Thus, describing the CPR response as a function of phase angle may be a way to determine relative age between deposits. Here, we examine the ejecta of eight Copernican aged craters and document CPR characteristics as a function bistatic angle in order to test that hypothesis. The spatial resolution of the data varied from one observation to another, as a function of the viewing geometry, but averaged ~100 m.

Four of the examined craters exhibit CPR characteristics suggestive of an opposition effect in S-band: higher CPR at lower bistatic (phase) angle (Figure 1). X-band observations of Anaxagoras also suggest an opposition surge at low bistatic angle, though relatively constant CPR in S-band at higher bistatic angles. The increase in CPR occurs near 2-4 degrees bistatic angle. These craters occur in both highlands and mare regions, and are all characterized as young. Three other examined craters exhibit CPR that remains relatively constant across phase angle. This may be for a couple reasons. 1) The craters are older (though still Copernican), and so the opposition effect will be less pronounced, or 2) there are few observations of these craters, with none to few over very small angles. An opposition effect may be present, and not yet observed. Both Schomberger A and Kepler exhibit unique scattering properties as a function of bistatic angles, with areas of relatively constant CPR at various CPR values. Continuing observations are targeting these regions to increase the phase angle coverage. Additional study is ongoing to fully characterize the CPR response with viewing geometry for these young craters. All of these targets will also be targeted in X-band, as well as adding additional craters (e.g., Schomberger, Copernicus).

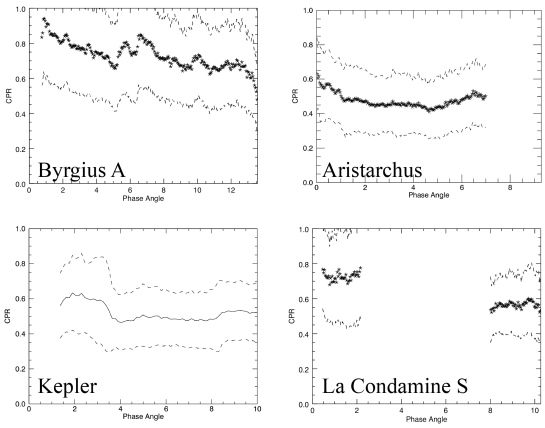

Figure 1. CPR as a function of phase for 4 examined craters. All four craters here exhibit differences in CPR with bistatic angle, with higher CPR at lower bistatic angles (characteristic of an opposition effect).

Acknowledgements

This work was funded by the NASA LRO and Mini-RF projects.

References

[1] Hapke et al. (1998), *Icarus*, 133, 89-97; [2] Nelson et al. (2000), *Icarus*, 147, 545-558; [3] Piatek et al. (2004), *Icarus*, 171, 531-545. [4] Campbell et al. (2010), *Icarus*, 208, 565-573; [5] Raney et al. (2012), *JGR,* 117, E00H21; [6] Carter et al. (2012), *JGR,* 117, E00H09; [7] Campbell (2012), *JGR*, 117, E06008; [8] Raney, R. K. et al. (2011), *Proc. of the IEEE*, 99, 808-823; [9] Black et al. (2001), *Icarus*, 151, 167-180;[10] Patterson, et al. (2017), *Icarus*, 283, 2-19; [11] Morota et al. (2009) *Met. Planet. Sci.* 44(8), 1115-1120; [12] Koenig et al. (1977) *Proc. LPSC*, 8, p. 555; [13] Baldwin (1985) *Icarus* 61, 63-91; [14] Ulrich (1969) USGS Map I-604(LAC-11)

EPSC Abstracts
Vol. 11, EPSC2017-506, 2017
European Planetary Science Congress 2017

ShadowCam – Seeing in the Dark

M.S. Robinson (1), P. Mahanti (1), L.M. Carter (2), B.W. Denevi (3) N.M. Estes (1) M.A. Ravine (4) E.J. Speyerer (1) and R.V. Wagner (1)
(1) Arizona State University, Tempe, AZ, USA (robinson@ser.asu.edu), (2) University of Arizona, Tucson, AZ, USA, (3) Johns Hopkins Applied Physics Laboratory, Laurel, MD, USA, (4) Malin Space Science Systems, San Diego, CA, USA.

Abstract

ShadowCam is designed to acquire high resolution, high signal-to-noise ratio (S/N) images within permanently shadowed regions (PSRs) on the Moon. The ShadowCam investigation has a single overarching goal: obtain measurements that directly address three of the four lunar volatile strategic knowledge gaps (SKGs) outlined in the NASA Korean Polar Lunar Orbiter (KPLO) instrument solicitation [**1**]. To this end we have five objectives: 1) identify albedo patterns in PSRs and interpret their nature, 2) investigate the origin of anomalous radar signatures associated with some polar craters, 3) document and interpret any temporal changes of PSR albedo, 4) map the morphology of PSRs to search for and characterize landforms that may be indicative of permafrost-like processes, 5) provide hazard and trafficability information within PSRs for future landed elements.

1. Introduction

ShadowCam has high heritage to the Lunar Reconnaissance Orbiter Camera (LROC) Narrow Angle Camera (NAC) [**2**], which typically acquires images with 50 to 100 cm pixel scale and S/N >100 (for illuminated regions). ShadowCam will use a build-to-print copy of the LROC NAC optics; a 700 mm focal length, f/3.6 Ritchey-Chretien telescope with a composite metering structure and baffle. The electronics will be modified from LROC to use a time delay integration (TDI) charge coupled device (CCD) detector with larger pixels than LROC NAC to increase the effective photon collection per pixel to more than 800 times that of the LROC NAC. ShadowCam has a 17-μradian pixel scale and a swath width of 2.8°. The maximum downtrack dimension of a ShadowCam image is 81,920 lines (buffer limited), but typical observations will be less than 20,000 lines. From a nominal 100 km altitude, ShadowCam will provide a pixel scale of 1.7 m over a ~5 km wide swath. With the increased integration time enabled by the TDI detector, these images will have a S/N greater than 100 within most PSRs. This S/N estimate has been validated by images taken by the LROC NAC of PSRs (pixel scales of 10 to 40 m and S/N ~20). While these LROC images are inadequate to address the goals of the NASA Advanced Exploration Systems, they do provide key engineering data about illumination conditions within PSRs and thus required instrument sensitivity. These LROC NAC observations drove the design of ShadowCam, ensuring that the measurement objectives will be met. Development of uplink, downlink and archive operations and procedures will rely heavily on those already developed for the LROC NAC experiment.

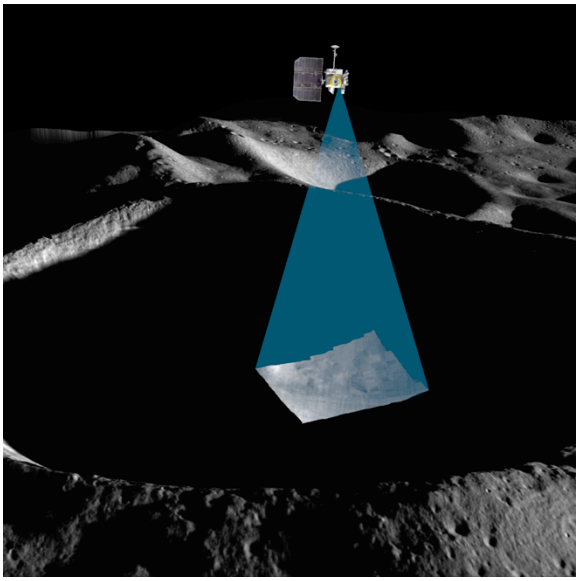

Figure 1. ShadowCam will image inside PSRs using secondary illumination reflected from nearby Sun-facing topographic facets.

2. Observations

ShadowCam will acquire complete coverage of PSRs poleward of 81°, which will enable mapping of landforms inside PSRs as well as the identification of

any albedo signatures indicative of surface frost. During the respective "polar summer," when the Sun is highest along the horizon and the amount of scattered light into the PSRs is maximized, ShadowCam will obtain its highest S/N observations. During this period, geometric stereo observations can be collected (if allowed by the KPLO mission operations) to derive gridded topographic models at 6 m/pixel. For the opposite hemisphere in "winter" we will acquire observations of non-polar (< 81° N, S) PSRs greater than 10 km^2 and search for albedo changes with polar PSRs. As the mission progresses, ShadowCam will collect repeat observations of PSRs that can be compared to prior images to identify any large scale surface changes associated with the transport of volatiles. These repeat observations can also be compared to look for new impacts as well as secondary splotches indicative of churned regolith, giving insight to regolith properties and potentially the presence of ice [3,4].

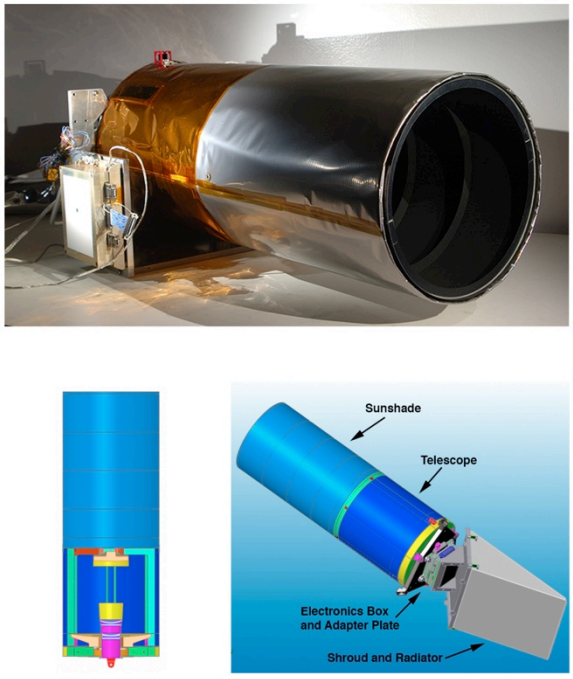

Figure 2. ShadowCam is based on the LROC NAC design shown above, and in engineering e-models (below).

ShadowCam can obtain complete coverage of the larger (>10 km^2) PSRs every month by imaging an average of 17,000 lines per orbit at the south pole and 10,000 lines per orbit at the north pole (assuming that at least 30% of each image contains not-previously-imaged PSR terrain; the rest is temporarily-shadowed terrain, illuminated terrain, or PSR terrain imaged on a previous orbit). Since the distribution of PSRs is not uniform, the number of lines needed per orbit varies, to a maximum of 78,000 lines on one pass over the south pole. The ShadowCam buffer can hold 256 MB (81,920 lines) before requiring a 35 m transfer to spacecraft memory, sufficient for 100% coverage of PSRs > 10 km^2 pole-ward of 81° for one orbit, and on an average orbit only 21% of the on-camera storage is needed. The remainder will be allocated for coverage of temporarily shadowed regions adjacent to PSRs for texture and albedo comparisons, for PSR or shadow observations at lower latitudes, for same-month repeat coverage of near-pole PSRs, and for calibration sequences, all subject to constraints on the total downlink volume.

While the NAC provides coverage of illuminated areas, ShadowCam will provide images of the shadowed areas. ShadowCam mosaics will be merged with the LROC NAC mosaics to make complete maps of the inside and outside of craters that host PSRs. These merged map products will put us one step closer to enabling landers and rovers to investigate the enigmatic lunar PSRs.

Acknowledgements
We thank NASA and KARI for the opportunity to build, fly and operate ShadowCam.

References

[1] NASA solicitation NNH12ZDA006O-KPLO, 2016.

[2] Robinson et al., *Space Sci. Revs*. 150, 81-124, 2010.

[3] Robinson et al., *Icarus*, 252, 229-235, 2015.

[4] Speyerer et al., *Nature*, doi:10.1038/nature19829, 2016.

EPSC Abstracts
Vol. 11, EPSC2017-547, 2017
European Planetary Science Congress 2017

Latest Bernese advances in Lunar geodesy

S. Bertone (1), D. Arnold (1), V. Girardin (1), A. Jäggi (1), and L. Mervart (2)
(1) Astronomical Institute of the University of Bern, Switzerland (stefano.bertone@aiub.unibe.ch), (2) Institute of Advanced Geodesy, Czech Technical University, Prague (CZ)

Abstract

The NASA mission GRAIL (Gravity Recovery And Interior Laboratory [1]) inherits its concept from the GRACE (Gravity Recovery And Climate Experiment) mission to determine the gravity field of the Moon. The Ka-Band Range Rate (KBRR) inter-satellite data allows for a highly accurate estimation of the lunar gravity field on both sides of the Moon [2], which is crucial to improve the understanding of its internal structure and thermal evolution. In this presentation we discuss our latest GRAIL-based lunar gravity fields generated with the Celestial Mechanics Approach [3, 4] using the Bernese Software (BSW, [5]). We provide independent solutions based on an optimal combination of one- and two-way Doppler and KBRR data iterated from the pre-GRAIL SGM150J gravity field. Finally, we compare our solutions for several geodetic parameters to other groups and to Lunar Laser Ranging (LLR) and we provide some preliminary results of our analysis.

1. Orbit: data, modeling and parametrization

Based on one-way X band and two-way S-band Doppler data, we perform orbit determination by solving six initial orbital elements, dynamical parameters, and stochastic parameters in daily arcs using a least-squares adjustment. We recently implemented an accurate modeling of non-gravitational forces, including accelerations due to solar and planetary [7] (albedo and IR) radiation pressure, based on the 28-plate macromodel developed by [8] to represent the GRAIL satellites. Empirical and pseudo-stochastic parameters are estimated on top of our dynamical modeling to absorb its deficiencies. We analyze the impact of different parametrizations using either pulses ($i.e.$, instantaneous velocity changes) and piecewise constant accelerations (PCA) on our orbits.

Based on these improved orbits, one- and two-way Doppler and KBRR data are then used together with an appropriate weighting for a combined orbit and gravity field determination process.

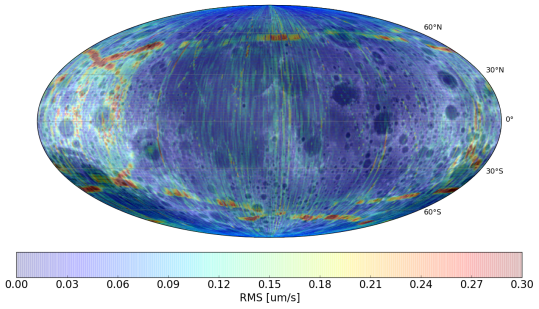

Figure 1: Root Mean Square (RMS) of KBRR residuals using a weighted combination of two-way Doppler and KBRR data, GRGM900C background field and a modeling of non-gravitational forces (solar and lunar radiation pressure) acting on GRAIL satellites. Residuals on most areas are close to the nominal KBRR accuracy of 0.03 μm/s, while correlations with topography are still visible. The sistematic signal at mid-latitudes shall be removed by a more accurate evaluation of light/shadow transitions.

2. Gravity field and tidal coefficients solutions

We present our latest independent solutions of the lunar gravity field, where KBRR data and Doppler one-way and two-way observations from the primary mission phase (PM, March-May 2012) are used. We present our analysis of an optimal combination of all data types on Normal Equations (NEQ) level. Both solutions based on the recent GRAIL GRGM900C gravity field [6] (as validation of our modeling and parametrization) and on iterations from the SELENE SGM150J gravity field (to check the independence of our solution) are presented. We detail our procedure to gradually enlarge the parameter space while adding

new data to our gravity field solution. A solution up to d/o 420, comparable to the first GL420 solution [1] by NASA JPL, is achievable with the computational power available on the UBELIX cluster at the University of Bern and with our parallel processing pipeline (based on Intel BLAS/MKL) within the BSW. In addition, we present our latest solution for the Moon tidal Love number k_2. We compare all of our results from the PM with the most recent solutions of the lunar gravity field and of other geodetic parameters released by other groups or obtained using other data and techniques ($e.g.$, LLR).

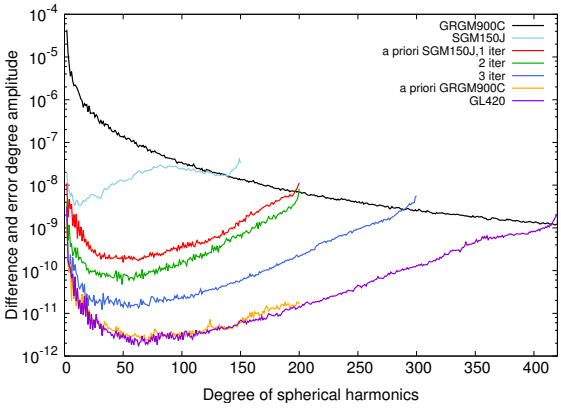

Figure 2: Difference degree amplitudes w.r.t. GRGM900C of 1. iterated solutions from SGM150J with progressively enlarged parameter space; 2. a solution based on GRGM900C up to d/o 600; 3. several reference solutions.

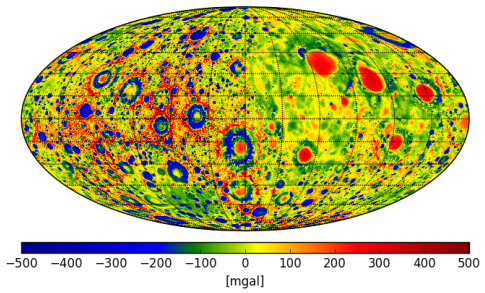

Figure 3: Free-air gravity anomalies on a $0.5^o \times 0.5^o$ grid of our d/o 300 iteration from SGM150J (Mollweide projection centered around 270^o, with the near-side on the right).

3. Summary and Conclusions

We present our most recent solutions for the lunar gravity field and tidal coefficient k_2, where further improvements have been obtained from the introduction of an accurate modeling of non-gravitational forces, an improved data screening and the optimisation of the parametrisation. We review the impact of different empirical orbit parametrizations and combination of data types on the recovery of lunar geodetic parameters. We show that the lunar gravity field can be recovered with a high quality by adapting the Celestial Mechanics Approach, even when using pre-GRAIL gravity field solutions as a priori. Our latest developments and the experience gained with GRAIL open the way to further research projects in planetary geodesy at AIUB and within ongoing collaborations with other groups.

Acknowledgements

We are grateful to the Planetary Data System (PDS) team for making GRAIL tracking data available. This study has been funded with the support of the Swiss National Science Foundation (SNSF).

References

[1] Zuber, M. T. et al.: Gravity Field of the Moon from the Gravity Recovery and Interior Laboratory (GRAIL) Mission, Science, 2013.

[2] Asmar, S. W. et al.: The Scientific Measurement System of the Gravity Recovery and Interior Laboratory (GRAIL) Mission, Space Science Reviews, 2013.

[3] Beutler, G. et al.: The celestial mechanics approach, Journal of Geodesy, 2010.

[4] Arnold, D. et al.: GRAIL gravity field determination using the Celestial Mechanics Approach, Icarus, 2015.

[5] Dach, R. et al.: Bernese GPS Software - Version 5.0, Astronomical Institute, University of Bern, 2007.

[6] Lemoine, F. G. et al.: High-degree gravity models from GRAIL primary mission data, Journal of Geophysical Research (Planets), 2013.

[7] Floberghagen, R. et al.: Lunar Albedo Force Modeling and its Effect on Low Lunar Orbit and Gravity Field Determination, ASR, 1999

[8] Fahnestock, E. G. et al.: Spacecraft thermal and optical modeling impacts on estimation of the GRAIL Lunar Gravity Field, AIAA/AAS Conference, 2012.

EPSC Abstracts
Vol. 11, EPSC2017-575, 2017
European Planetary Science Congress 2017

Spectrally Distinctive Material Excavated by the Imbrium Basin on the Moon

R. Klima (1), D. Buczkowski (1), C. Ernst (1), B. Greenhagen (1), N. Petro (2) and M. Shusterman (1)
(1)Johns Hopkins University Applied Physics Laboratory, Laurel, MD, USA (2) NASA/Goddard Space Flight Center, Greenbelt, MD, USA. (Rachel.Klima@jhuapl.edu / Fax: +1-443-778-8939

Abstract

It has long been recognized, from telescopic and orbital data, that some of the massifs surrounding the Imbrium basin excavate noritic material. This material has generally been interpreted as possible Mg-suite norites, either ejected or uplifted during the Imbrium basin-forming impact. With new orbital data, it has become clear that there is great spectral diversity in the massifs. We will examine the spectral properties of these massifs and examine the lithological contacts between materials of different composition to better constrain the crustal provenance of these materials.

1. Introduction

As an early crystallizing mineral, orthopyroxene provides important clues for understanding the evolution of the lunar surface, from the earliest magma ocean cumulates, through the anorthositic flotation crust, to later stage intrusive magmatism. Using data from the Moon Mineralogy Mapper (M^3) to search for Mg-suite norites, concentrations of low-Ca, high-Mg pyroxene have been characterized around the Imbrium and Apollo Basins [1]. These deposits may be exposures of Mg-suite plutons, may represent excavated material from deeper within the primary lower crust or mantle, or may be remnants of melt sheets (differentiated or undifferentiated). Iron-rich orthopyroxenes have been identified elsewhere, in smaller craters throughout the highlands crust.

The Imbrium basin has been extensively studied for many years [e.g., 2-3]. Though the bulk of the basin is flooded by mare basalts, massifs consisting of more generally feldspathic material surround the edges of Mare Imbrium in the northwest, northeast, and southeast (Fig. 1). Telescopic measurements of Apennine mountains revealed regions spectrally dominated by orthopyroxene or pigeonite [3]. Later radiative transfer modeling of Clementine data suggested that Mg-suite-like norites may surround much of the Imbrium basin [4]. In the initial global to have the highest Mg# were found in the Montes Alpes region near Vallis Alpes [1].

The Imbrium basin is large enough to have excavated between 60-85 km into the Moon [3], deep enough to penetrate through the crust and into the mantle. It is also associated with the strongest thorium detections by Lunar Prospector [5], and is likely to be rich in KREEP [6].

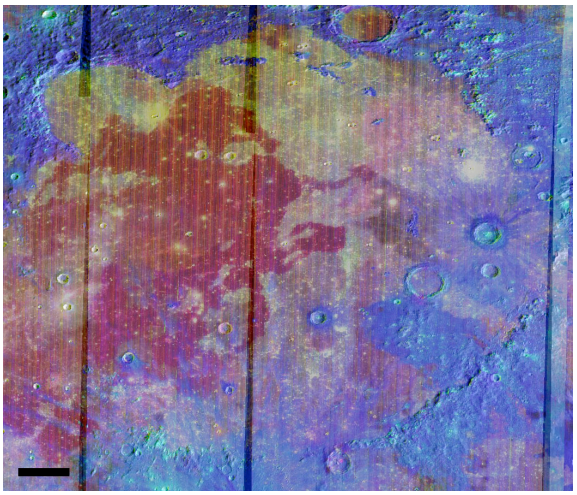

Figure 1: M3 standard color composite (R=integrated 1 μm band depth, G=integrated 2 μm band depth, B=1.58 μm reflectance). Orthopyroxene-rich regions appear as cyan. The highest concentration of Mg-rich orthopyroxene is in the massifs of Montes Alpes (NE corner). The center of Imbrium basin is located at 32.8°N 15.6°W and the scale bar is 100 km across.

2. Geological Occurrence and Spectral Properties of Imbrium Massifs

Orthopyroxenes around the boundary of the Imbrium basin are primarily associated with material mapped as crater slope material or undifferentiated terra material [eg. 7-8]. This material occurs throughout

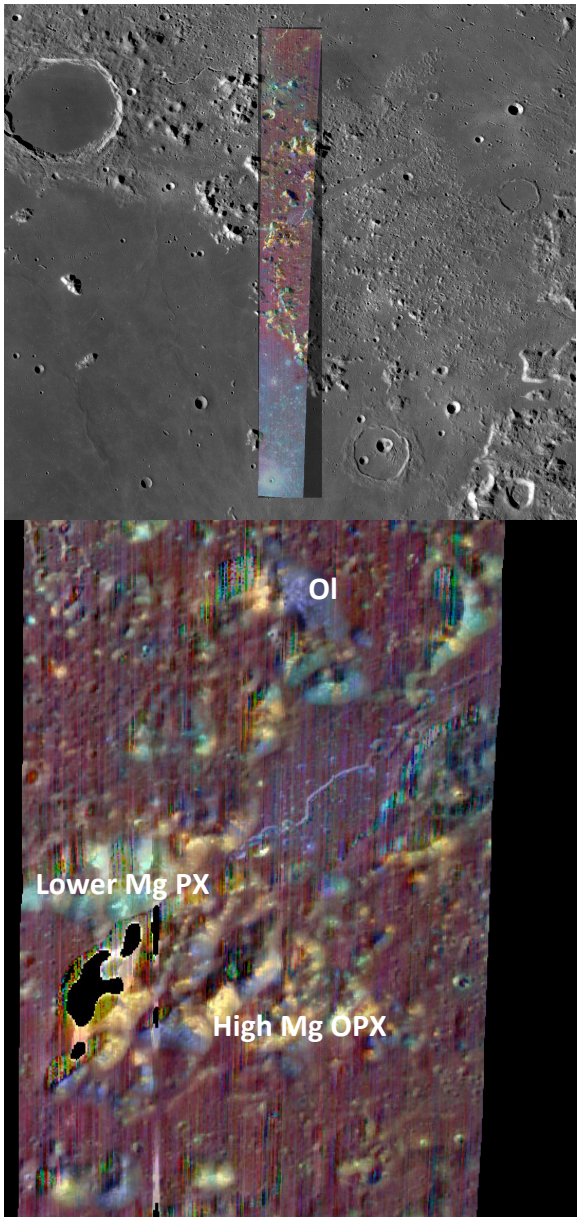

Figure 2: (top) Context image and (bottom) full resolution color composite of a section of Montes Alpes highlighting pyroxene diversity (R= 1.9 μm band depth, G=integrated 2 μm band depth, B= integrated 1 μm band depth).

the Alpes formation, which has been interpreted as deformed pre-Imbrium material, and Fra Mauro formation, which is defined as thick basin ejecta. The massifs in which the orthopyroxenes are found are primarily distinguished from the surrounding formations by their occurrence on steep slopes and their medium to high albedo, and their origin, as currently mapped, may be either uplifted material or crater ejecta. Using a color composite designed to highlight the diversity in pyroxene compositions (Fig. 2), it is clear that the massifs in the Montes Alpes are not dominated by a single lithology. High-Mg orthopyroxene, olivine, and a second pyroxene—either higher iron orthopyroxene or more Ca-rich pyroxene, are located in immediate contact with one another on the ~10 km-scale massifs.

3. Summary and Next Steps

Work is currently underway to search for the lithological boundaries at higher resolution using LROC imagery. The specific mineralogy of the deposits is being investigated by a combination of NIR spectral modeling and by incorporating measurements taken by the Diviner thermal infrared spectrometer. Diviner data will be used to analyze the position of the Christiansen feature (CF). The CF shifts in wavelength depending on the silicate polymerization of the bulk rock being measured, and is thus extremely effective at distinguishing relative proportions of minerals in a two-component mixture of a highly polymerized silicate such as anorthite and a less polymerized silicate such as pyroxene. Though fine-grained materials in the NIR and in the vibrational Reststrahlen bands are nonlinear, mixing at the CF have been shown to be essentially linear [9]. The assumption of linear mixing of endmember CFs may cause uncertainties in absolute mineral abundances of up to ~10% but will not affect relative abundances between sites [e.g. 10].

Acknowledgements

We are grateful to the NASA LDAP program for supporting this work under grant # NNX16AN50G and to the LRO project for support to N. Petro.

References

[1] Klima, R. L., et al. (2011), JGR, doi:10.1029 /2010JE003719. [2] Wilhelms D. E. et al. (1987), The geologic history of the moon, USGS, Washington, D.C.[3] Spudis, P., et al., (1988), LPSC XVIII, 155. [4] Lucey, P. G. and J. T. S. Cahill (2009), LPSC XL, #2424. [5] Lawrence, D. J. et al. (1998), Science, 281, 1484-1489. [6] Jolliff et al. (2000), JGR, 105, 4197. [7] Page, N. J. (1970) *U.S.G.S.* Map I-666. [8] M'Gonigle, J. W. and Schleicher, D. (1972) *U.S. G.S.* Map I-701. [9] Arnold, J.A. and Glotch, T.D. (2014), LPSC XLV, #2470. [10] Greenhagen, B. T. et al. (2014), LPSC XLV, #2641.

EPSC Abstracts
Vol. 11, EPSC2017-604, 2017
European Planetary Science Congress 2017

Wave activities resulted from Solar wind-Moon interaction

A. Skalsky (1) and **A. Sadovski** (1,2)
(1) Space Research Institute (IKI RAS), Moscow, Russia, (2) National Research University Higher School of Economics, Moscow, Russia (asadovsk@iki.rssi.ru / Fax: +7-495-3331248)

Abstract

Direct interaction of the solar wind with lunar regolith, void at night side of Moon and anomalously magnetized regions at lunar surface lead to the variety of wave phenomena in the near Moon environment. The present paper is aimed to overview wave observations from the previous missions and wave generation mechanisms. Particular attention is pointed on mini-magnetospheres formed above the magnetized areas at Moon surface and related wave observations.

1. Introduction

On the first sight the lunar plasma environment seems to be very simple matter. However the Moon-plasma system interactions show the complexity and variability of the physical processes. Moreover interactions have a kinetic nature and the kinetic theory is necessary for their studying.

The solar wind interaction with Moon surface and environment has received many attention last years. The regions of enhanced crustal magnetic field (magnetic anomalies) were found. In such regions magnetic field may attain several hundred nT [1, 2, 3]. The formation and dynamics of such anomalies are far from the understanding. Also the observations of Kaguya and Chandrayaan revealed significant deflected proton fluxes over magnetic anomalies. Such proton fluxes allow to imply that the magnetic anomalies may act as magnetosphere-like obstacles (mini-magnetospheres), modifying the upstream plasma [4, 5]. The observations of energetic neutral atoms also confirm the existence of the enhanced fluxes of deflected particles.

Variety of electric fluctuations was observed during the passage of Wind spacecraft across the lunar wake: langmuir waves, electrostatic modes above electron cyclotron frequency, whistlers. The investigations by Kuncic and Cairns [6] revealed emissions on plasma frequency and its first harmonic. Electron reflection at quasi-shock at leading edge of magnetic anomaly could drive the electric field oscillations. The generation mechanism is similar to that known for foreshock of planetary bow shock.In KAGUYA and Lunar Prospector missions the monochromatic whistlers near the Moon were observed as narrow band magnetic fluctuations with frequencies close to 1 Hz, and are mostly left-hand polarized in the spacecraft frame.

We review different mechanisms for wave generation in plasma environment near such mini-magnetosphere regions.

2. Magnetic anomalies at the Moon

There are three main models for the formation of the magnetic anomalies. The first one is the active lunar core dynamo [7]. However this model has several unresolved questions: time scale, chemical and thermodynamical evolution of the core, albedo swirls. The second one is impact model [8] which has problems with different times for plasma currents (5 min), internal seismic waves (8 min), surface seismic waves (80 min), the vagueness of the magnetic field values, central magnetic anomalies, albedo. The last one is comet impact model [9]. However its main problem is comet impact rate.

3. Wave activity near the Moon

During the passage of Wind spacecraft across the lunar wake it was observed the variety of electric fluctuations. For example, langmuir waves, electrostatic modes above electron cyclotron frequency, whistlers [10]. The investigations by Kuncic and Cairns [6] revealed emissions on plasma frequency and its first harmonic. In KAGUYA [11] and Lunar Prospector [12] missions the monochromatic whistlers were observed which are generated by the solar wind interaction with lunar crustal magnetic anomalies. Also KAGUYA observed large-amplitude monochromatic ULF waves [13] with periods of 120–100 s and amplitudes about 3 nT. The direction of the propagation of the waves is not exactly parallel to the interplanetary magnetic field.

4. Solar wind interaction with magnetic field anomalies

The measurements by Lunar Prospector show that the surface magnetic field may be represented by dipole and in interaction with the solar wind shock-like structure should be formed [3]. If the reflection takes place on such structure it may be similar to the reflection on the shock wave (see discussion in [3], where the authors have shown that for the Imbrium anomaly some kind of shock wave can exist). However many observations show that the mini-magnetosphere in many cases doesn't form.

In papers [14, 15] the simple model for the ion reflection from anomaly was presented. The main conclusion was that the some shock structure may forms and great deflection of electrons is possible. However, presented model of reflection may be appropriate only for strong magnetic anomalies and the amount of deflected ions should be very sensitive to the solar wind conditions.

5. Summary and Conclusions

The measurements and existing models sows that the waves can exist in wide frequency range. Wave phenomena observed at the Moon are mostly associated with the wake boundary and lunar crust magnetic anomalies.

References

[1] Coleman, P.J., Lichtenstein, B.R., Russell, C.T. et al.: Magnetic fields near the moon, Proc. Lunar Planet. Sci. Conf. Vol. 3, pp. 2271, 1972.

[2] Lin, R.P.: Constraints on the origins of lunar magnetism from electron reflection measurements of surface magnetic fields, Phys. Earth Planet. Int. Vol. 20, pp. 271, 1979.

[3] Lin, R.P., Mitchell, D.L., Curtis, D.W., et al.: Lunar surface magnetic fields and their interaction with the solar wind: Results from Lunar Prospector, Science, Vol. 281, pp. 1480–1484, 1998.

[4] Futaana, Y., Barabash, S., Holmström, M., Bhardwaj, A.: Low energy neutral atoms imaging of the Moon, Planet. Space Sci., Vol. 54, pp. 132–143, 2006.

[5] Wieser, M., Barabash, S., Futaana, Y. et al.: First observation of a mini-magnetosphere above a lunar magnetic anomaly using energetic neutral atoms, Geophys. Res. Lett., Vol. 37, pp. L015103, 2010.

[6] Kuncic, Z., Cairns, I.H.: Radio emission from mini magnetospheres on the Moon. Geophys. Res. Lett., Vol. 31, pp 11, 2004.

[7] Stegman, D.R., Jellinek, A.M., Zatman, S.A. et al.: An early lunar core dynamo driven by thermochemical mantle convection, Nature, Vol. 421, pp. 143—146, 2003.

[8] Hood, L.L. and Huang, Z.: Formation of magnetic anomalies antipodal to lunar impact basins: Two-dimensional model calculations, J. Geophys. Res., Vol. 96, p. 9837, 1991.

[9] Shevchenko V.V. in Contemporary problems of mechanics and physics of the space (in russian). M., Fizmatlit, 2003.

[10] Kellogg P.J., Goetz K., Monson S.J. et al.: Observations of plasma waves during a traversal of the Moon's wake, Geophys. Res. Lett., Vol. 23, pp. 1267–1270, 1996.

[11] Tsugawa Y., Terada N., Katoh Y. et al.: Statistical analysis of monochromatic whistler waves near the Moon detected by Kaguya, Annales Geophysicae, Vol. 29, pp. 889–893, 2011.

[12] Halekas J.S., Brain D.A., Mitchell D.L., Lin R.P.: Whistler waves observed near lunar crustal magnetic sources, Geophys. Res. Lett., Vol. 33, pp. L22104, 2006.

[13] Nakagawa T., Nakayama A., Takahashi F. et al.: Large-amplitude monochromatic ULF waves detected by Kaguya at the Moon, J. Geophys. Res., Vol. 117, pp. A04101, 2012.

[14] Sadovski A.M., Skalsky A.A.: Coupling of earth's magnetosphere, solar wind and lunar plasma environment, Adv. Space Res., Vol. 54, pp. 2017—2020, 2014.

[15] Skalsky A.A., Sadovski A.M.: Reflection of solar wind protons from magnetic anomalies of the moon, Cosmic Research, Vol. 53, pp. 70–73, 2015.

EPSC Abstracts
Vol. 11, EPSC2017-689-1, 2017
European Planetary Science Congress 2017

Lunar impact flashes: estimation of their temperatures.

C. Avdellidou and D. Koschny
Scientific Support Office, Directorate of Science, European Space Research and Technology Centre (ESA/ESTEC), 2201 AZ Noordwijk, The Netherlands (chrysa.avdellidou@esa.int)

Abstract

Here we present the calculation of the temperatures of the impact flashes detected on the lunar surface. This is done for the first time since the beginning of the lunar obervations, thanks to an ESA-funded project. We believe that these observations in combination with on-going hypervelocity impact experiments will lead to a better understanding of the collisional processes.

1. Lunar Impact flashes

Almost 20 years ago the lunar surface started to be monitored with small telescopes for the detection of collisions by recording the produced light [1]. The initial purpose was to understand the flux of impactors on Earth. Since the Earth's atmosphere is a great interference and the sky monitoring systems for bolides did not have so large detection area, the lunar surface provides an extended area for numerous detections. The estimation of the flux of near Earth Objects (NEOs) is important not only for the prevention of human civilisation (meter-sized, see Chelyabinsk event in 2013) but also for the protection of the space assets (cm-sized objects). Apart from the NEO flux per se, the lunar surface becomes a *large-scale impact laboratory*, considering both the impactor sizes and speeds compared to the indoor laboratory hypervelocity experiments [2] where the sizes of impactors are typically a few mm and the speeds below 10 km/s.

Impact flash data are valuable for several other purposes [3].

- Find the coordinates on the lunar surface that the flash occured and earch for the crater afterwards.
- Calculate the luminous efficiency of a flash.
- Estimate the mass of the NEO, when a safe assumption of the impact speed can be made. This can be more safelly done from flashes caused by a meteor stream, where the impact speed can be better constained.

2. Observations

The European Space Agency (ESA) is directing and funding lunar observations at Kryoneri in Peloponnese, Greece [4]. The facilities that belong to the National Observatory of Athens, were recently upgraded. An 1.2 m telescope is equiped with two identical Andor Zyla sCMOS cameras. A dichroic beam-splitter directs the light on to the two cameras, that observe in visible and inrfared wavelengths using R_c and I_c Cousin filters respectively. Currently it is the largest telescope in the world that performs dedicated observations, surveying lunar impact flashes. The novelty of this instrumentation setup is that it aquaires data from two detectors simultaneously. In that way there is no need anymore of using two different telescopes to perform sychronous observations, in order to reject the false detections (e.g.cosmic rays).

Observations are scheduled and performed each month when the Moon is in favorable phase. Data are stored and callibrated immediately after the end of the observations. Each night standard stars at similar airmass are also observed in both filters. This procedure is executed by the specialised NELIOTA pipeline that was developed for this particular type of observations.

After obtainining the lunar data and the raw data of the standard stars we used our own routines for data reduction and photometry deriving the fluxes for the flash and standard stars. Our analysis is primarily focused on the calculation of the flash temperatures for a first time using data from big scale impacts via telescopic observations.

3. Temperature Estimations

To begin with, because the first data obtained come from sporadic objects we focused on the flash temperature, T_f calculation. This is now possible for a first time after the beginning of the lunar observations, since obervations are performed in two wavelengths. Although an impact flash is not a product of the same physics laws as the luminocity of a star, we will work

on our analysis by assuming a black body behaviour. By using the fluxes of the standard star in both wavelengths we can callibrate the fluxes of the flash and solving the Planck equation derive the T_f.

4. Implications

Generally, when a collision occurs there is a partitioning of the kinetic energy of the impactor. However there are a numerous parameters that play a role on that and thus we are still not fully aware of this procedure. So far scientists had to use as flash temperatures values from literature that were usually obtained from laboratory experiments. Now we can have a better understaning, especially when the T_f is coupled with mass and speed estimation of the impactor. In addition, the observations are done with high time resolution (30 fps) and this enables us to detect any "anomalies" in the flash light-curve tail (and also evolution of the temperature) during the cooling phase of the hot plasma in the ejecta. This will help to get insight and try to assign this phenomenon to a natural cause, e.g. either to secondary impacts by the ejecta or to the changes of the opacity of the ejecta plum. Finally from this work we can have a first idea, in large scales, how the mass and/or speed of the colliding body affects the flash duration and the difference we detect in visible and infrared wavelengths. Complementary hypervelocity impact experiments are designed by us in order to mimic the observations.

Acknowledgments

We would like to thank Alceste Bonanos (PI of NELIOTA) and the rest of NELIOTA team.

References

[1] Ortiz, J.L. et al.: Optical detection of meteoroidal impacts on the Moon, Nature, Volume 405, Issue 6789, pp. 921-923, 2000.

[2] Burchell, M.J. et al.: Light Flash and Ionization from Hypervelocity Impacts on Ice, Icarus, Volume 122, Issue 2, pp. 359-365, 1996.

[3] Suggs, R.M. et al.: The flux of kilogram-sized meteoroids from lunar impact monitoring, Icarus, Volume 238, p. 23-36, 2014.

[4] Bonanos A. Z. et al., NELIOTA: ESA's new NEO lunar impact monitoring project with the 1.2m telescope at the National Observatory of Athens, IAU Symposium 318, 327-329, 2016.

EPSC Abstracts
Vol. 11, EPSC2017-693-3, 2017
European Planetary Science Congress 2017

Numerical simulation of illumination and thermal conditions at the lunar poles using LOLA DTMs

P. Gläser (1), D. Gläser (2), J. Oberst (1,3) , G. A. Neumann (4) , E. Mazarico (4), M. A. Siegler (5)
(1) Technical University Berlin, Dept. of Planetary Geodesy, 10623 Berlin, Germany (philipp.glaeser@tu-berlin.de)
(2) University of Stuttgart, Dept. of Hydromechanics and Modelling of Hydrosystems, 70569 Stuttgart, Germany
(3) German Aerospace Center, Dept. of Planetary Geodesy, 12489 Berlin, Germany
(4) NASA Goddard Space Flight Center, Code 698, Greenbelt, MD 20771, USA
(5) Planetary Science Institute, Tucson, Arizona 85719, USA

Abstract

A numerical simulation of the lunar illumination and thermal environment was carried out for near-polar regions. As the foundation of this study high-resolution, twenty meters per pixel and 400 x 400 km large polar Digital Terrain Models (DTMs) were derived from Lunar Orbiter Laser Altimeter (LOLA) data. Illumination conditions were simulated by synthetically illuminating the LOLA DTMs using the horizon method considering the Sun as an extended source [1,6,7]. Areas receiving almost constant illumination near areas in permanent shadow were identified as potential exploration sites for future missions. Further, at each position the found illumination is used as an input to evaluate the one-dimensional heat equation for the upper two meters of regolith. First results seem to be in good agreement with heat maps created from the Diviner Lunar Radiometer Experiment (DLRE), most commonly known as Diviner.

1. Introduction

The lunar polar regions are the only regions on the Moon where Permanently Shadowed Regions (PSRs) can be found. This stems from the small 1.54° lunar rotational obliquity which in turn leads to extreme polar illumination conditions. Hence, directly at the poles the Sun appears to only move $\pm 1.54°$ about the horizon where crater floors are likely to be PSRs and crater rims and topographic highs in contrast receive extended illumination. PSRs were long predicted to exist and also to contain water-ice concentrations [2] which was now supported by several more recent studies [3,4,5]. Due to the proximity of possibly water-rich PSRs next to almost constant illuminated areas the lunar poles are a prime exploration target for future missions relying on solar power. This study focuses on a 50 x 50 km area centered on each pole using illumination data [6,7] to evaluate surface and sub-surface regolith temperatures as expected at candidate landing sites and nearby PSRs.

2. Method

Polar LOLA DTMs of 400 x 400 km and twenty meters per pixel were created to derive illumination for the central 50 x 50 km subsets while taking into account the far-field topography. Modeling polar illumination with the horizon method as described in [1,6] and using it as an input at each time-step (2 h), the heating of the lunar surface and subsequent conduction in the sub-surface can be evaluated. At surface level we balance the incoming insolation with the sub-surface conduction and radiation into space, whereas in the sub-surface we consider conduction with an additional constant radiogenic heat source at the bottom of our two-meter layer. Density is modeled to be depth-dependent, the specific heat parameter to be temperature-dependent and the thermal conductivity to be depth- and temperature-dependent. We implemented a fully implicit finite-volume method in space and backward Euler scheme in time to solve the one-dimensional heat equation at each pixel in our 50 x 50 km DTM. Due to the non-linear dependencies of the parameters mentioned above, the Newton's method is employed as the non-linear solver together with the Gauss-Seidel method as the iterative linear solver in each Newton iteration. The software is written in OpenCL and runs in parallel on the GPU which allows for fast computation of large areas and long timescales.

3. Results

To start the numerical calculation of the surface temperatures, initial temperature values given for a certain

time need to be supplied. We chose our simulation to start on January 1, 2010 with a homogeneous temperature distribution of 100 K in the respective upper two meter layer. The simulation determines the current illumination every two hours which serves as the input for the numerical temperature calculation. Since the homogeneous initial temperature values are far from reality the simulation needs some time to converge into a realistic temperature distribution. In our preliminary study we ran the simulation for a total of almost two years (23 months, 8300 steps), with the final heat map dating from December 1, 2011 (see Fig. 1). Where Diviner data are available, we compared temperature measurements with our model results which are in good agreement and will help refine our parameters.

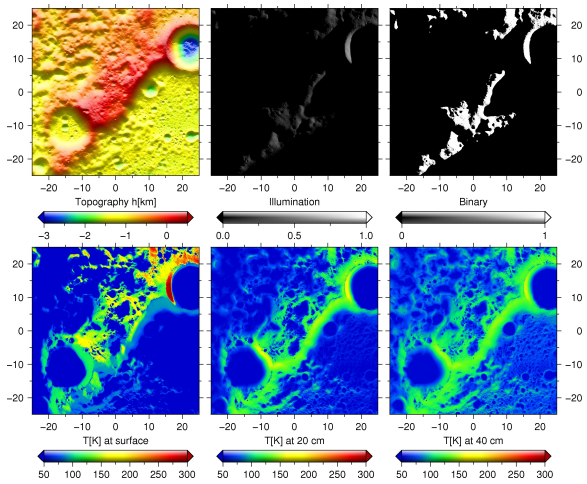

Figure 1: Top: LOLA DTM of the north pole (left), simulated illumination at December 1, 2011 18:00:00 UTC (middle), binary illumination (right). Bottom: Surface heat map (left), 20 cm sub-surface heat map (middle), 40 cm sub-surface heat map (right). All maps have a resolution of 20 m/pix and are presented in gnomonic map projection.

4. Summary and Conclusions

We successfully implemented a numerical model to solve the heat equation on the GPU in parallel which allows us to derive lunar polar temperature maps for any given time. First results are consistent with Diviner but further improvements to our model are necessary. As a next step we intend to incorporate the effect of scattered sunlight which might add a significant amount to the heat balance in the PSRs.

Acknowledgements

This project was funded by a grant of the German Research Foundation (GL 865/2-1). We also gratefully acknowledge the support of NVIDIA Corporation with the donation of the Quadro M5000 GPU used for this research.

References

[1] Mazarico, E. et al.: Illumination conditions of the lunar polar regions using LOLA topography, Icarus, Vol. 211, pp. 1066-1081, 2011.

[2] Watson, K., Murray, B., Brown, H.: On the possible presence of ice on the Moon. Journal of Geophysical Research 66, 1598–1600, 1961.

[3] Mitrofanov, I. et al.: Testing polar spots of water-rich permafrost on the Moon: LEND observations onboard LRO. Journal of Geophysical Research (Planets), 117, 2012.

[4] Spudis, P.D. et al.:. Evidence for water ice on the moon: Results for anomalous polar craters from the LRO Mini-RF imaging radar. Journal of Geophysical Research (Planets) 118, 2016–2029, 2013.

[5] Miller, R.S., Lawrence, D.J., Hurley, D.M.: Identification of surface hydrogen enhancements within the Moon's Shackleton crater. Icarus 233, 229–232, 2014.

[6] Gläser, P. et al.: Illumination conditions at the lunar south pole using high resolution Digital Terrain Models from LOLA. Icarus 243, 78–90, 2014.

[7] Gläser, P. et al.: Illumination conditions at the lunar poles: Implications for future exploration, LRO Special Issue PSS (submitted), 2017.

EPSC Abstracts
Vol. 11, EPSC2017-751, 2017
European Planetary Science Congress 2017

The dust environment of airless planetary bodies

M. Horányi(1,2), J. Szalay (3), X. Wang(1,2)
(1) Department of Physics and Laboratory for Atmospheric and Space Physics, U. of Colorado, CO, USA
(2) NASA-SSERVI: Institute for Modeling Plasmas, Atmospheres, and Cosmic Dust (IMPACT), U. of Colorado, CO, USA
(3) Southwest Research Institute, San Antonio, TX, USA

Abstract

The Moon, as all airless bodies in the solar system, is continually bombarded by interplanetary dust particles, it is also immersed in the solar wind plasma flow and UV radiation. There are several controversial observations from the Apollo era that can now be revisited due to new spacecraft data, and recent dedicated laboratory experiments. Hypervelocity dust impacts generate secondary dust ejecta particles, neutral and ionized gases, sustaining the recently discovered, permanently present dust cloud engulfing the moon, and contributing to the production of the dilute lunar atmosphere and ionosphere. UV and plasma exposure results in the electrostatic charging of the lunar regolith, that can lead to the mobilization, transport, and large-scale redistribution of the lunar fines. We focus on the recent results of in situ observations, as well as the latest laboratory results, a combination which resulted in a much improved understanding of the lunar dust environment, and its expected similarity to the surfaces of other airless planetary bodies.

1. Dust measurements in space

The Lunar Dust Experiment (LDEX) on board the Lunar Atmosphere and Dust Environment Explorer mission was designed to make in situ dust measurements while orbiting the Moon [1, 2]. Particles with radii $a \geq 0.3$ μm were detected as impacts [3]. LDEX was also capable of measuring the collective signal generated from dust impacts with sizes below its single-particle detection threshold. A putative population of electrostatically lofted grains above the lunar terminator with radii of approximately 0.1 μm has been suggested to exist since the Apollo era. LDEX performed the first search with an in situ dust detector for such a population. Fig.1 shows the LDEX observations taken over the lunar terminator indicating no evidence of electrostatically lofted grains in the altitude range of 3 - 250 km above the lunar terminator, with an upper limit of 40-100 cm^{-}3 [3, 4]. This has also been supported by the remote sensing observations of the Clementine and LRO missions [5, 6]. Contrary to these observations, the LADEE UVS instrument's [7] spectral data did suggest the existence of at least an intermittent nanodust exosphere at the Moon containing a population of particles sufficiently dense to be detectable via scattered sunlight. Near the peak of the Quadrantid meteoroid stream the observed negative spectral slope is consistent with backscattering of sunlight by nanodust grains with radii less than 20 to 30 nm [8]. This population is suggested to be generated by impacts during the Quadrantid stream, similar to the enhancements observed by LDEX during this and other shower periods [3, 9]. While to date there is no evidence of high-altitude lofted dust due to electrostatic effects over the lunar surface, there is strong supporting evidence from recent laboratory experiments that dust charging can lead to significant effects near the surface of an airless planetary body.

2. Laboratory experiments

New laboratory experiments shed light on dust charging and transport that have been suggested to explain a variety of unusual phenomena on the surfaces of airless planetary bodies. Lofted large aggregates and surface mobilization are related to many space observations. New experiments (Fig.1) have successfully shown that the emission and re-absorption of photoelectrons and/or secondary electrons at the walls of micro-cavities formed between neighboring dust particles below the surface are responsible for generating unexpectedly large negative charges and intense particle-particle repulsive forces to mobilize and lift off dust particles [10, 11].

3. Summary and Conclusions

This talk will summarize the LADEE/LDEX results identifying the permanently present and intermittently

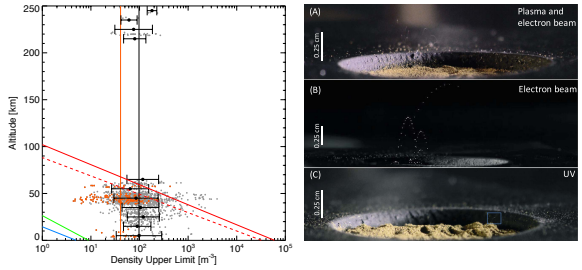

Figure 1: *Left*:The upper limit of the density of dust particles as a function of altitude, derived from the LDEX current measurements. Each gray dot represents a terminator crossing. Black dots show the averages in 10 km increments. The orange points indicate LDEX measurements taken in Earth's magnetotail [4]. *Right*: Images of dust transport and hopping trajectories in (a) plasma and electron beam, (b) electron beam, and (c) UV experiments. A blue square highlights a hopping trajectory captured under UV illumination. Deposits of dust particles on the surface outside the crater also indicate their hopping motions in all three images. Large aggregates up to 140 μm in diameter are lofted in addition to individual particles in the range of 38 - 45 μm in diameter [10].

enhanced lunar dust ejecta cloud that is sustained by the continual bombardment by interplanetary dust particles originating form the sporadic background population, as well as the meteoroid streams. The measurements indicate no high-altitude dust density enhancements over the terminator regions, as it was anticipated due to dust charging and strong electric fields in this region. However, there is strong supporting evidence for efficient dust mobilization and transport near the surface, a process that is likely to be responsible for the observed dust ponding on asteroids [12].

References

[1] R. C. Elphic, G. T. Delory, B. P. Hine, P. Mahaffy, M. Horányi, A. Colaprete, M. Benna, and S. Noble, "The Lunar Atmosphere and Dust Environment Explorer (LADEE) Mission," *Space Science Reviews*, 2014.

[2] M. Horányi, Z. Sternovsky, M. Lankton, C. Dumont, S. Gagnard, D. Gathright, E. Grün, D. Hansen, D. James, S. Kempf, B. Lamprecht, R. Srama, J. R. Szalay, and G. Wright, "The Lunar Dust Experiment (LDEX) Onboard the Lunar Atmosphere and Dust Environment Explorer (LADEE) Mission," *Space Science Reviews*, vol. 185, pp. 93–113, Dec. 2014.

[3] M. Horányi, J. R. Szalay, S. Kempf, J. Schmidt, E. Grün, R. Srama, and Z. Sternovsky, "A permanent, asymmetric dust cloud around the Moon," Nature, vol. 522, pp. 324–326, June 2015.

[4] J. R. Szalay and M. Horányi, "The search for electrostatically lofted grains above the Moon with the Lunar Dust Experiment," *Geophys. Res. Lett.*, vol. 42, no. 13, pp. 5141–5146, 2015.

[5] D. A. Glenar, T. J. Stubbs, J. M. Hahn, and Y. Wang, "Search for a high-altitude lunar dust exosphere using Clementine navigational star tracker measurements," *Journal of Geophysical Research (Planets)*, vol. 119, pp. 2548–2567, Dec. 2014.

[6] P. D. Feldman, D. A. Glenar, T. J. Stubbs, K. D. Retherford, G. Randall Gladstone, P. F. Miles, T. K. Greathouse, D. E. Kaufmann, J. W. Parker, and S. Alan Stern, "Upper limits for a lunar dust exosphere from far-ultraviolet spectroscopy by LRO/LAMP," *Icarus*, vol. 233, pp. 106–113, May 2014.

[7] A. Colaprete, K. Vargo, M. Shirley, D. Landis, D. Wooden, J. Karcz, B. Hermalyn, and A. Cook, "An Overview of the LADEE Ultraviolet-Visible Spectrometer," Space Sci. Rev., vol. 185, pp. 63–91, Dec. 2014.

[8] D. H. Wooden, A. M. Cook, A. Colaprete, D. A. Glenar, T. J. Stubbs, and M. Shirley, "Evidence for a dynamic nanodust cloud enveloping the Moon," *Nature Geoscience*, vol. 9, pp. 665–668, Sept. 2016.

[9] J. R. Szalay and M. Horányi, "Detecting meteoroid streams with an in-situ dust detector above an airless body," Icarus, vol. 275, pp. 221–231, Sept. 2016.

[10] X. Wang, J. Schwan, H. Hsu, E. Grün, and M. Horányi, "Dust charging and transport on airless planetary bodies," Geophys. Res. Lett., no. DOI: 10.1002/2016GL069491, 2016.

[11] J. Schwan, X. Wang, H.-W. Hsu, E. Grün, and M. Horányi, "The charge state of electrostatically transported dust on regolith surfaces," Geophys. Res. Lett., vol. 44, pp. 3059–3065, Apr. 2017.

[12] J. E. Colwell, A. A. S. Gulbis, M. Horányi, and S. Robertson, "Dust transport in photoelectron layers and the formation of dust ponds on Eros," Icarus, vol. 175, pp. 159–169, May 2005.

EPSC Abstracts
Vol. 11, EPSC2017-752, 2017
European Planetary Science Congress 2017

The CE5 scientific data products using pds4

X. Tan (1,2), X.X.Zhang (1,2)
(1) National Astronomical Observatories, Chinese Academy of Sciences,Beijing ,China., (2)Key Laboratory of Lunar and Deep Space Exploration,National Astronomical Observatories, Chinese Academy of Sciences,Beijing China. (tanx@nao.cas.cn)

Abstract

The Chang'e 5(CE5) will be launched in 2017. The CE5 data will be archived and distributed to the scientific community through the CNSA's ground research and application system (GRAS). All data will be compliant with NASA's Planetary Data System (PDS4) standards for formatting and labelling files. This paper summarizes the format and content of the CE5 data products and associated metadata.

1. CE5 Scientific Payloads

The CE5 spacecraft consists of four modules - a Service Module, a Return Vehicle, the Lander and the Ascent Vehicle. And the are four payloads are equipped on the lander, who are the Panoramic Camera (PCAM), the Descending Camera (LCAM), Lunar Regolith Penetrating Radar(LRPR) and Lunar Mineralogical Spectrometer(LMS), which will investigate the geological structures and minerals compositions of the sampling area, and integrate exploration of the structure of landing site interior.

2. PDS4.0

PDS4 is an object-oriented system based on a central Information Model, from which everything within the system is defined explicitly. This differs greatly from PDS3 and provides continuity across discipline nodes, which has not been present in the past.
PDS4 is product-centric. A "product" is defined as a label file and the object (data, document, etc.) it de-scribes.The new system replaces the use of ODL (man-aged by JPL/Caltech, used only by PDS) with eXtensi-ble Markup Language (XML)[1].
There are four fundamental data structures that may be used for archiving data in the PDS. All products delivered to the PDS must be constructed from one or more of these structures. These four fundamental structures are described using four base classes: Array (used for homogeneous Ndimensional arrays of scalars), Table_Base (used for repeating records of heterogeneous scalars), Parsable_Byte_Stream (a stream of bytes that can be parsed using standardized rules), and Encoded_Byte_Stream (an encoded stream of bytes). All other digital object classes in the PDS are derived from one of these four base classes.[2]
The PDS4 Data Dictionary (DD), which is an ad-junct to the PDS4 Information Model (IM), define classes and attributes used in PDS4 XML files by spec-ifying tags, their meanings, and the acceptable values (including structure) that may appear as content. The key words can be used to provide all of the information required to access and analyse the data. [3]

3. CE5 Data Products

Change's data product are categorized into three levels including level 0, level 1 and level 2. [4] Only Level1 and Level2 data products are compliant with NASA's Planetary Data System (PDS) Standards. Level1 data are uncorrected, and Level 2 data are further processed with radiometric calibration, approximate geometric correction, photometric calibration, etc.. One basic CE5 product includes one or more data objects and their lable. For each product, there is only one lable to describe the contents and format of each individual product. The Introduction of the CE5 data products are as follows:

3.1data lable

CE5 data lables are followed the general structure which is defined by the PDS4. We give the attribute value of each class according to the PDS Data Dictionary. As above mentioned, the mission specific classes and attributes are defined in CE5 local data dictionary, and these information are described in mission area- a subclass of the Observation_Area.

3.2data object

In CE5 mission, one or two data objects constitute a single observation, one is the main observation data(for example one or more image), the other (if there)is the auxiliary telemetry data, which prefix the

observation data.The data structure of each payload are as follows(see table1). i)We use the Array_3D_Image to store multiple image, the three dimensions are respectively time, line and samples. The Array_3D_Image are also used to storage a color image.(i.e. PCAM Level 2C data product is a color image which have a color restoration and color correction, based on level 2B data.). ii) We use the Table_Binary to store the LRPR data. iii) We use the Table_Character to store the spectral data and the auxiliary telemetry parameter.

Table 1: data structure of each payload

	Level1	Level 2A	Level2B	Level2C
PCAM	Array_3D_Image Table_Character	Array_2D_Image		Array_3D_Image
LCAM	Array_3D_Image	Array_2D_Image		none
LRPR	Table_Binary			
LMS (Visible band)	Array_3D_Image Table_Character			none
LMS (medium wave, shortwave, and near infrared band)	Table_Character			

3.3local data dictionaries.

In CE5 mission, the data products are followed with PDS Data Dictionary Version 1.5.0.0. Beyond that, we also maintain our own 'CE5 Data Dictionary', appending many of our own 'local data dictionaries' to specify information pertinent only to individual CE5 mission.

Ten classes are defined in CE5 Data Dictionary, they are:

Work_Mode_Parm: Describes the parameters associated with the scientific payload work mode, including exposure_mode, automatic_exposure_mean_gray, exposure_gear, gain, etc..

Instrument_Parm: Describes the parameters of the sensor, including focal_length, pixel_size, principle_point_coordinate, etc..

Processing_Parm: Describes the coefficient of the data processing model for each level.

Lander_Location: The longitude, latitude and the reference_frame are given in this class.

Grid_Point_Location: The longitude and latitude with the row and column numbers where they form a subclass, to describe the location of the grid point in moon coordinate system.

Vector_Cartesian_3_Position: The Cartesian 3D position of antenna1 to antenna12 for LRPR are given in this class.

Vector_Cartesian_3_Pointing: The observation vector of four corner point and center point are given in this class.

Exterior_Orientation_Elements: The camera center position and rotation angle are given in this class.

Besides this, the pitch and yawing are given in "Rotation_angle" class as a attribute. And the incidence angle, azimuth angle and phase angle of four corner point and center point are given in "Angle_pointing_results" class.

References

[1] Neakrase L. D., Huber L. F., Beebe R. F., et al.(2014) LPSC 45th , Abstract #1417.

[2] PDS Standards Reference 1.4.0 (2015).

[3] PDS4 Concepts Version 1.4.0(2015).

[4] Tan, X., Liu, J. J., Li, C. L., Feng, J. Q., Ren, X., Wang, F. F., ... & Zhang, Z. B. (2014). Scientific data products and the data pre-processing subsystem of the Chang'e-3 mission. Research in Astronomy and Astrophysics, 14(12), 1682.

EPSC Abstracts
Vol. 11, EPSC2017-787-1, 2017
European Planetary Science Congress 2017

A CubeSat mission for Moon and its vicinity exploration

M.Lavagna (1), F.Ferrari(1), P.Lunghi (1), Anna Milillo(2), Ernesto Palomba(2), E. De Angelis (2), S. Orsini (2), Claudio Labanti(3), Simone Dell'Agnello(4), Primo Attinà(5), Guido Parissenti(5)

(1) Politecnico di Milano-Aerospace Science and Technology Dept.-Milano, Italia (michelle.lavagna@polimi.it)

(2) National Institute of Astrophysics/ Institute of Space Astrophysics and Planetology, Roma, Italia (anna.milillo@iaps.inaf.it, ernesto.palomba@iaps.inaf.it)

(3) Istituto Nazionale di Astrofisica-Istituto di Astrofisica Spaziale e Fisica Cosmica, Bologna, Italia (labanti@iasfbo.inaf.it)

(4) Istituto Nazionale di Fisica Nucleare, Frascati, Italia (Simone.DellAgnello@lnf.infn.it)

(5) GP Advanced Projects srls, Giussago (BS), Italia (guido.parissenti@gpadvancedprojects.com)

Abstract

The LUnar Cubesat Initiative Aimed to Novel and Unique Science (LUCIANUS) is a CubeSat mission concept focused on the Moon and its proximity.

In last years, increasing miniaturization and energetic efficiency in payload design has made CubeSat systems attractive for scientific missions and in orbit demonstrations, not only in the vicinity of the Earth, but also in deep space environment. LUCIANUS proposes to demonstrate these new capabilities in a cis-lunar scientific mission, composed by the ARDAN and BARBICANE sub-missions to cover different scientific and technological challenges.

ARDAN consists in two identical 8U CubeSats, 14 kg margined mass, released at 500km and capable to get their operational orbit independently; ARDAN s/c orbit on a sequences of circular Lunar orbit (100km; 76km and 41km) sequentially lowered to allow different, and increasing resolutions in the data acquisition. The overall maneuvers cost less than 200 m/s and the strategy allows covering the Moon surface every 15 days. ARDAN trajectory design is led by the on-board science: this sub-mission aims at lunar resource prospecting and environment analysis, each one equipped with an IR camera, VISTA (a miniaturized thermogravimetry analyser) and ALENA (Analyser for Lunar Energetic Neutral Atoms), a reduced version of the ELENA sensor for ENA mapping on board of the BepiColombo; both the latter proposed by INAF-IAPS.

The IR camera records subtle thermal gradients on the lunar surface to detect, map and characterize in size lunar lava tubes; VISTA and ALENA detect the distribution of suspended dust and neutral atoms, to study their interactions with light magnetic fields and solar radiations which drive ARDAN to fly at very low altitude.

BARBICANE is a single 12U CubeSat, 21 kg margined mass, equipped with miniaturized Gamma Ray Bursts (GRB) detector. The spacecraft would orbit on a Near Rectilinear Orbits (NRO) in the Moon-Earth Three-Body System – 15800 x 85000 km wide - to prospect the vehicle behavior in those, never exploited, non-keplerian trajectories. NRO are interesting location in the Moon Village framework, as they are suitable for supporting surface vehicles from the Moon surface to cis-lunar outpost continuous transfer back and forth.

BARBICANE would embark VISTA payload as well: during the raising of the spacecraft, from 500km release altitude to NRO, VISTA will provide high altitudes dust distribution data - complementary to ARDAN -.

LUCIANUS space segments are all equipped with Corner Cube Reflectors to tightly track their positions.

LUCIANUS mission aims at supporting and complementing the lunar exploration goals currently identified by the scientific community, involving a fleet of CubeSats: such small satellites exploitation

allows increasing the surface coverage and the mission robustness. Scientific objectives and technological challenges are presented in the paper, together with the mission timeline and phases. The preliminary design solutions identified to address the scientific and technological goals are discussed at system and subsystem levels to demonstrate the LUCIANUS mission feasibility by exploiting already off-the-shelf components to be shortly ready to launch.

Miniaturized solutions are proposed for all subsystems, particularly for propulsion and ADCS. Details on the design are provided for all subsystems and the budgets are eventually presented.

References

[1] M.Lavagna, S.Rafano Carnà, Earth-Moon multipurpose orbiting infrastructure, paper no.AAS, 16-488 26th AAS/AIAA Space Flight Mechanics Meeting, February 14-18, 2016 Napa, California

[2] L.Bucci, M.Lavagna, IAC-16,C1,9, Periodic orbit-attitude solutions along planar orbits in a perturbed circular restricted three-body problem for the Earth-Moon system, International Astronautical Congress, Sept 26-30, 2016, Guadalajara-Mexico

[3] Vetrisano M., Lavagna M., Grasso M., A in Situ Resource Utilisation Demonstrator for the Moon: Preliminary Design and Dynamic Model, 58th International Astronautical Congress 2007, Hyderabad, India, 24-28 Sept. 2007, ISBN: 9781605601502, p. 7172-7173

[4] D. Scaccabarozzi, B. Saggin, M. Tarabini, E. Palomba, A. Longobardo, E. Zampetti, Thermo-mechanical design and testing of a quartz microbalance for space applications, Advances in Space Research, 54, 11, 2386-2397, 2014

[5] Orsini et al., SERENA: a suite of four instruments (ELENA, STROFIO, PICAM and MIPA) on board BepiColombo-MPO for particle detection in the Hermean Environment, BepiColombo Special Issue on Planetary and Space Science, 58, 166-181, 2010

[6] Milillo et al., Exosphere generation of the Moon investigated through a high-energy neutral detector

[7] M. Martini, S. Dell'Agnello, et al., MoonLIGHT: A USA–Italy lunar laser ranging retroreflector array for the 21st century, Planetary and Space Science 74 (2012) 276–282.

EPSC Abstracts
Vol. 11, EPSC2017-801, 2017
European Planetary Science Congress 2017

Statistical analysis of the magnetization signatures of lunar impact basins

L. R. Gabasova (1), M. A. Wieczorek (2)
(1) University of Paris-Saclay, France (l.r.gabasova@gmail.com), (2) Côte d'Azur Observatory, France

Abstract

Studying the magnetic signatures of lunar impact basins allows us to reconstitute the global magnetic field at the time of their formation and further constrain the period of activity of the core dynamo, which is currently believed to have been active before 3 Ga [1]. While there have been qualitative studies of the distribution of these magnetic signatures as a function of the basin age [2, 3], they do not incorporate new data from the SELENE and GRAIL missions, nor do they perform a rigorous statistical analysis. Here, we quantify the magnetic signatures of the largest lunar impact basins using this new data as well as robust statistical bounds.

1. Data

This study uses digital elevation maps created with data from LOLA to identify the basins as well as lunar magnetic field strength maps produced by [4], at a resolution of 2 pixels per degree. From these, we produce equal-area grids with constant latitude and variable longitude spacing to allow for accurate statistical analysis. We study all the lunar impact basins with a radius greater than 200 km (74 in total).

2. Method

As magnetic anomalies associated with basins tend to have radial symmetry, we produce radial profiles for each basin by binning the data according to distance from the basin center. Data within 1.5 basin radii is used to produce the profiles. We define the following areas within each profile, normalized over the basin radius R: within the peak ring ($0 - 0.5R$), within the main ring ($0 - 1R$) and outside the main ring ($1 - 1.5R$).

Using the mean magnetic field strength $< |B| >$ of these areas we define a statistic M representing the strength of the basin's magnetic anomaly, defined in one of two ways (the distinction being made visually):

1. If the magnetic anomaly appears to be confined to the peak ring, then:

$$M = \frac{< |B| >_{0-0.5R}}{< |B| >_{1-1.5R}} \quad (1)$$

2. If the anomaly extends over the entire basin, then:

$$M = \frac{< |B| >_{0-1R}}{< |B| >_{1-1.5R}} \quad (2)$$

We calculate the value of M for all basins, and classify the results according to the sign and/or presence of a magnetic signature. The statistical bounds are established via Monte Carlo modeling as described below.

2.1. Synthetic maps

To establish a base distribution with which the observed results are to be compared, we generate a set of synthetic maps. To do this, we work with the spherical harmonic expansion of the magnetic field strength map: assuming a Gaussian distribution, we calculate the power spectrum of the original map, which we use to generate a map with the same statistical properties as the observed data. This process is repeated 10000 times, and M is calculated for each basin's location in the synthetic maps, which gives us a base statistical dispersion and thus the cutoff threshold for defining a statistical anomaly. We calculate the probability of obtaining the observed M value for each basin using the cumulative distribution function for the synthetic M values. For basins where $p < 0.05$ we have a magnetic anomaly: the basin is magnetized if $M > 1$, demagnetized otherwise.

3. Results and discussion

Figure 1 shows the M and p values for all the basins with a known stratigraphic age group (36 of the total 74) as defined by [5]: from 1 (youngest) to 15 (oldest). Figure 2 shows the distribution of basin magnetic

signatures in the three major lunar geological periods (known for 38 basins): Imbrian (corresponding to age groups 1-3), Nectarian (4-6) and pre-Nectarian (7-15). We can see that the magnetic signature of a basin strongly depends on its age: early pre-Nectarian basins are chiefly neutral (with some positive and negative signatures), while nearly 40% of Nectarian basins are strongly magnetized and all Imbrian basins are demagnetized. This is partially coherent with earlier publications [1, 2]: the early Nectarian magnetization peak is consistent with the theorized early activity of the core dynamo. The strong demagnetization of Imbrian basins, however, is at odds with the Apollo sample paleo-intensity measurements. Our results are susceptible to bias from the following sources:

- The signatures of larger and older basins have significant overlap with those of smaller craters;
- As only large basins were studied, the sample size is quite small especially where Imbrian basins are concerned.

We expect to continue this study by extending the dataset to smaller impact craters to correct some of the above biases and produce a more precise analysis. We will also attempt to correlate the basin statistics with the corresponding magnetization causes.

Acknowledgements

Funding for L. Gabasova's 2016 internship was provided by the Institut de Physique du Globe de Paris (IPGP).

References

[1] Weiss, B. P., Tikoo, S. M.: The lunar dynamo. Science 346 (6214), 1246753, 2014.

[2] Halekas, J. S., Lin, R. P., Mitchell, D. L.: Magnetic fields of lunar multi-ring impact basins. Meteoritics & Planetary Science 38 (4), 565–578, 2003.

[3] Halekas, J. S., Mitchell, D. L., Lin, R. P., Hood, L. L., Acuña, M. H., Binder, A. B.: Demagnetization signatures of lunar impact craters. Geophysical Research Letters 29 (13), 2002.

[4] Tsunakawa, H., Takahashi, F., Shimizu, H., Shibuya, H., Matsushima, M.: Surface vector mapping of magnetic anomalies over the Moon using Kaguya and Lunar Prospector observations. Journal of Geophysical Research: Planets 120 (6), 1160–1185, 2015.

[5] Wilhelms, D. E., John, F., Trask, N. J.: The geologic history of the Moon. Technical report, 1987.

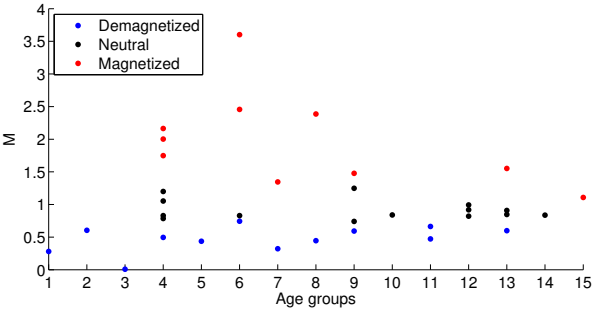

(a) M value as a function of age group.

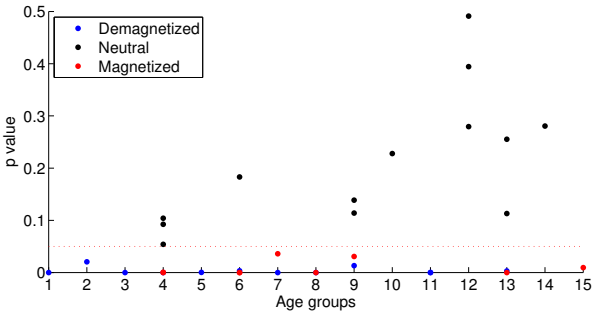

(b) p value as a function of age group.

Figure 1: Basin statistics as a function of age group, with magnetization thresholds calculated from synthetic data.

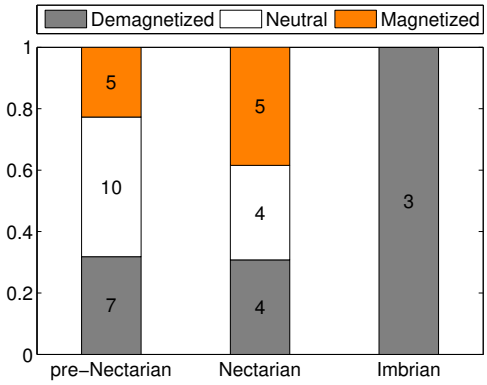

Figure 2: Distribution of magnetic field signatures in the major lunar geological periods. The number in each box denotes the total number of basins of that type and age.

EPSC Abstracts
Vol. 11, EPSC2017-913, 2017
European Planetary Science Congress 2017

Trapping of atmospheric gases during crushing of lunar samples

A. B. Verchovsky (1), J. Mortimer (1), A. I. Buikin (2) and M. Anand (1, 3)
(1) The Open University, Milton Keynes UK, (2) Vernadsky Institute RAS, Moscow, Russia, (3) Natural History Museum, London, UK (sasha.verchovsky@open.ac.uk)

Abstract

Experimental simulation of trapping of atmospheric noble gases and nitrogen during crushing of lunar samples using an electromagnetic metal crusher demonstrates that nitrogen is trapped much more efficiently than noble gases. This observation is in sharp contrast with lunar samples that display trapped terrestrial atmosphere-like noble gases, but do not contain terrestrial N, thereby suggesting another source for the atmosphere-like noble gases.

1. Introduction

The presence of terrestrial atmospheric noble gases in lunar samples has been known since the early analyses of lunar samples delivered by the Apollo program [1-4]. Some lunar samples contain trapped gases with clear terrestrial atmosphere Xe isotopic signatures [3, 4]. As part of the sample preparation procedure some of them have been crushed before analyses. Therefore, it was thought that trapping of the atmospheric gases occurred at this stage. However, the terrestrial atmospheric gases have been found also in the samples that have not been crushed prior to analysis [3]. Nevertheless, even in these cases the origin of the trapped gases has been attributed to terrestrial contamination, though the mechanism by which they are trapped remains unclear.

In the present study, we investigated this issue by taking into consideration nitrogen, which is the most abundant atmospheric constituent, and is also more chemically active than noble gases. Along with analyses of N in lunar samples which have an excess of atmospheric noble gases [5], we performed several crushing experiments to see in what proportion noble gases and nitrogen can be trapped and compared this with their abundance in the lunar samples.

2. Experimental

For the analyses of noble gases, nitrogen and carbon we used the 'Finesse' instrument [6], which allows simultaneous measurements of abundances and isotopic compositions of different species present. First, we analysed each sample as it is, using stepped combustion and then in the second experiment we employed vacuum crushing. More than 10000 strokes cumulatively were applied during crushing, resulting in production of a fine-grained powder. The crushed samples were subsequently removed from the crusher and an aliquot of the sample was then analysed by stepped combustion. The transfer from the crusher to the combustion furnace includes brief exposure of the crushed material to the atmosphere. In a third experiment, we crushed (3000 strokes) one of the samples (69921) under atmospheric conditions i.e. without evacuation of air from the crusher, and then analysed the crushed material using stepped combustion.

Altogether, three lunar soils (12070, 14141 and 69921) were used in this study. The nitrogen, carbon and noble gas step-combustion data for these samples have been published previously [7].

During crushing a metal powder has also been produced due to friction between the movable insertion and the walls of the crusher. This metal powder was mixed with the sample so tightly that it was not possible to separate them from each other using physical methods of separation. Perhaps the metal and sample particles have coalesced as a result of extreme heating and pressure raised at strokes. In order to account for the N contribution from the metal we have analysed the metal parts of the crusher and also performed a crushing experiment under vacuum with an empty crusher and collected the formed metal particles for further analysis. Analyses of the metal samples showed elevated concentrations of N in the metal.

3. Results and discussion

Based on our initial analysis of nitrogen in the lunar rock, 12064, which showed a clear excess of atmosphere-like Ne, we found [5] that the $(N_2/Ne)_{tr}$ ratio is lower than the terrestrial atmospheric ratio by

a factor of $6x10^4$. This indicates that atmospheric nitrogen is much less efficiently trapped by crushing than Ne, contradicting the general idea that chemically active atmospheric species should be trapped during crushing of silicate materials in air with higher efficiency than the inert ones. This result can be considered as evidence for a non-atmospheric origin of the trapped Ne in this sample.

The most important result of the crushing experiments is that in both cases, exposing the crushed material to air after crushing and crushing in air, shows a significant increase in N (by a factor of 6-14) concentrations in the crushed residues compared to the original samples. One of the most important questions is whether or not these high N concentrations can be explained by contribution from the crusher metal only. Analysis of possible concentrations of metal in the lunar soils after crushing and release patterns of N in the samples compared to that in the metal allows us to conclude that metal can explain a significant portion, but not all of the observed concentrations of N in the crushed lunar samples. A fraction of N significantly higher than that present in the original samples has been trapped during crushing.

The majority of solar noble gases are lost during both types of crushing, but the amounts of trapped atmospheric noble gases are extremely low and can barely be seen in the residual materials (Fig. 1). The $^{36}Ar/^{40}Ar$ ratio is a very sensitive indicator of the presence of atmospheric Ar, since this ratio in the samples analysed is significantly different from that in the atmosphere. The results shown in Fig. 1 indicate almost no difference in the $^{36}Ar/^{40}Ar$ ratio between the original and crushed samples in spite of a huge difference in $N_2/^{40}Ar$ ratio. N is trapped much more efficiently, however.

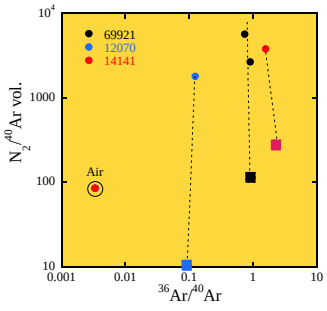

Figure 1: Bulk compositions of the original (squares) and crushed (circles) lunar soil samples.

4. Summary and Conclusions

Our crushing experiments demonstrated a very high efficiency of trapping for N, compared to that of noble gases. The mechanism of trapping and the source of N (apart from the fact that it comes from air) is not clear. However, what is clear is that lunar rocks with trapped atmosphere-like noble gases do not show such high concentrations of N and, therefore, their noble gases do not seem to have been trapped from air as a result of crushing.

Acknowledgements

The authors thank CAPTEM for the allocation of Apollo samples. This work was partially funded through a UK Science and Technology Facilities Council studentship to JM and a research grant to M.A (# ST/L000776/1).

References

[1] Lightner B. D. & Marti K.: Lunar trapped xenon, Proc. *5th LPSC*, 2023-2031, 1974

[2] Leich D. A. and Niemeyer S.: Trapped xenon in lunar anorthositic breccia 60015 *Proc. 6th LPSC*, 1953-1965, 1975.

[3] Niemeyer S. and Leich D. A.: Atmospheric rare gases in lunar rock 60015, *Proc. 7th LPSC*, 587-597, 1976

[4] Niedermann S. and Eugster O.: Noble gases in lunar anorthositic rocks 60018 and 65315: Acquisition of terrestrial krypton and xenon indicating an irreversible adsorption process, GCA *56*, 493-509, 1992.

[5] Mortimer J. et al.: Simultaneous analysis of abundance and isotopic composition of nitrogen carbon, and noble gases in lunar basalts: Insight into interior and surface processes on the Moon, *Icarus 255*, 3-17, 2014.

[6] Verchovsky A. B. et al.: Separation of planetary noble gas carrier from bulk carbon in enstatite chondrites during stepped combustion, *EPSL 199*, 243-255, 2002.

[7] Mortimer J. et al.: Predominantly non-solar origin of nitrogen in lunar soils, *GCA 193*, 36-53. 2016.

EPSC Abstracts
Vol. 11, EPSC2017-933, 2017
European Planetary Science Congress 2017

Radio science electron density profiles of lunar ionosphere based on the service module of circumlunar return and re-entry spacecraft

M. Wang (1), S. Han (2), J. Ping (1), G. Tang (2) and Q. Zhang (2)
(1) National Astronomical Observatories, Chinese Academy of Sciences, Beijng, China, (2) National Key Laboratory of Science and Technology on Aerospace Flight Dynamics, Beijng, China (wangmy@nao.cas.cn)

Abstract

The existence of lunar ionosphere has been under debate for a long time. Radio occultation experiments had been performed by both Luna 19/22 and SELENE missions and electron column density of lunar ionosphere was provided. The Apollo 14 mission also acquired the electron density with in situ measurements. But the results of these missions don't well-matched. In order to explore the lunar ionosphere, radio occultation with the service module of Chinese circumlunar return and reentry spacecraft has been performing. One coherent S-band and X-band radio signals were recorded by China deep space stations, and local correlation was adopted to compute carrier phases of both signals. Based on the above work, the electron density profiles of lunar ionosphere was obtained and analyzed.

1. Introduction

Since 1960s, radio occultation has been used in planet exploration to detect vertical changing of temperature, pressure and electron density of atmosphere and ionosphere. In 1966, the radio occultation experiment of Pioneer-7 proved the existence of Lunar ionosphere which is very thin (electron density is about $4*10^4$ el/cm^3)[8]. In Apollo 14 mission, the electron density detected by the Charged Particle Lunar Environment Experiment (CPLEE) was 10^4 el/cm^3 at several hundred meters high during lunar day time. In Luna-19 & 22 mission, the electron density profiles were detect and the peak densities were about 10^3 el/cm^3 [10]. In the last decade, European mission SMART-1 and Japanese mission SELENE also performed radio occultation experiment for Lunar ionosphere[1,6,7].

The circumlunar return and reentry spacecraft is a Chinese precursor mission for the Chinese lunar sample return mission. After the status analysis of the spaceborne microwave communication system, we confirmed that the frequency source of the VLBI beacon in X-band and the signal in S-band is provided by the same frequency source onboard the satellite and its short-term stability is n*10-9. Compared to the frequency source onboard SELENE whose short-term stability is n*10-7 [6], the service module provides a stable and reliable signal source for dual frequency radio occultation.

China deep space network measurement center has organized a series of radio occultation experiments which performed by Jiamusi and Kashi deep space station.

2. Radio experiment of the service module of the circumlunar return and reentry spacecraft

With the radio occultation technique, electromagnetic waves are transmitted from the spacecrafts to the Earth, passing through the atmosphere (either during a rise event or a set event as seen from the receiver), are refracted at an angle that is determined by the refractivity gradients along the path. The refractivity variation depends on the gradients of air density, water vapour and electron density (in this case, only electron density counts).

As seen in Fig. 1, the signal transmitted from the spacecraft in S and X band passed through Luanr ionosphere, interplanetary plasma, Earth ionosphere and atmosphere, finally received by the station. A hydrogen maser in the receiving station is used as the frequency reference source for open-loop radio experiments.

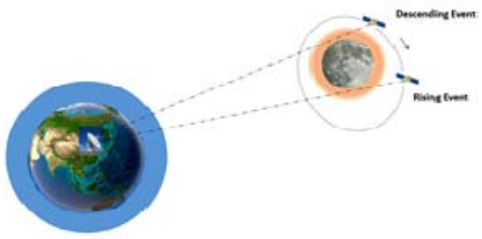

Fig. 1. The illustration of the service module of the circumlunar return and reentry spacecraft radio occultation experiment.

The signals transmitted from the spacecraft in S and X band passed through lunar ionosphere, interplanetary plasma, Earth ionosphere and atmosphere, finally received by the ground tracking stations. According to the coherent ratio of the S/X signal, we convert the phase information of S-band signal to the frequency of X-band signal and calculate the difference of these two signal. Then, the extrapolation algorithm was used here to deduct the interference error of the earth ionosphere and the interplanetary plasma. Based on the above work, the electron density profiles of lunar ionosphere was explored.

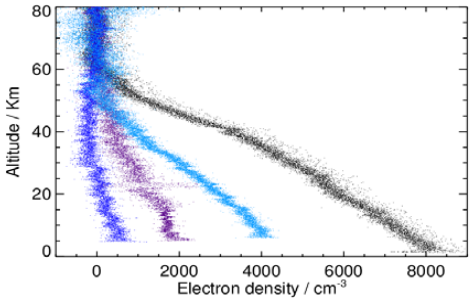

Fig2. The electron density profiles based on Radio experiment of the service module of the circumlunar return and reentry spacecraft.

The maximums of electron column concentrations are between $0.4\sim0.5\times10^{16}$ el/m^2, are two times of the maximum result from Luna 19/22, are 1~2 orders higher than the SELENE result, but well-matched with the result from CPLEE. These results show that the lunar ionosphere is clearly exist and much stronger than we expected. The result here gives a positive support and some dynamical constrains for the scientific objective of the very low frequency radio astronomical payload onboard the Chang'E-4 lander mission. But it also raises a new question that the characteristics and formation mechanism of a stronger lunar ionosphere is remain unknown. More observations will be performed for further scientific targets.

Acknowledgements

This work was supported in by the NSFC No.41590851.

References

[1] Y. Goto, T. Fujimoto, Y. Kasahara, A. Kumamoto, T. Ono, "Lunar ionosphere exploration method using auroral kilometric radiation," Earth Planets & Space, vol 63, pp. 47-56, 2011.

[2] T.J. Stubbs, D.A. Glenar, W.M. Farrell, et al., "On the role of dust in the lunar ionosphere," Planetary & Space Science, vol. 59, pp. 1659-1664, 2011.

[3] W.D. Daily, W.A. Barker, M. Clark, et al., "Ionosphere and atmosphere of the moon in the geomagnetic tail," Journal of Geophysical Research, vol. 82, pp. 5441-5451, 1977.

[4] J.S. Ping, Y.D. Huang, M.Y. Wang, et al., "The possibility of detection of Mars ionosphere by radio occultation (in Chinese)," Deep Space Exploration, vol. 2, pp. 18-25, 2007.

[5] M.J. Wu, P. Guo, X.G. Hu, et al., "Research on error analysis of ionosphere detection by radio occultation (in Chinese)". Annual publication of Shanghai Astronomical Observatory , Chinese Academy of Sciences, vol. 1, pp. 99-111, 2014.

[6] T. Imamura, K.I. Oyama, T. Iwata, Y. Kono, K. Matsumoto, Q. Liu, et al., "The possibility of studying the lunar ionosphere with the SELENE radio science experiment," Earth Planets Space, vol. 60, pp. 387-390, 2008.

[7] T. Imamura, T. Iwata, Z.I. Yamamoto, N. Mochizuki, Y. Kono, K. Matsumoto, et al., "Studying the lunar ionosphere with selene radio science experiment," Space Science Reviews, vol. 154, pp. 305-316, 2010.

[8] S. Pluchino, F. Schillirò, E. Salerno, G. Pupillo, G. Maccaferri, P. Cassaro, "Radio occultation measurements of the lunar ionosphere," Memorie Della Società Astronomica Italiana Supplement, vol. 12, pp. 53, 2008.

[9] A.S. Vyshlov, "Preliminary results of circumlunar plasma research by the Luna 22 spacecraft," Space Res, vol. 01, pp. 945-949, 1976.

EPSC Abstracts
Vol. 11, EPSC2017-961, 2017
European Planetary Science Congress 2017

Rocky outcrops and low crater densities on lunar wrinkle ridges: Evidence for recent tectonic activity?

A. Valantinas* (1), K. M. Kinch (1) and A. Bridžius (2,3)
(1) Niels Bohr Institute, University of Copenhagen, Denmark (*adomas.valantinas@gmail.com). (2) Vilnius University Observatory, Čiurlionio 29, 03100 Vilnius, Lithuania, (3) Center for Physical Sciences and Technology, Saulėtekio av. 3, 10257 Vilnius, Lithuania.

1. Introduction

Lunar wrinkle ridges are prominent elongated and topographically up to a few hundred meters high geologic features found in lunar maria [1,2]. Their formation is linked to a combination of folding and thrust faulting tectonic processes and are thought to have formed when the bulk of lunar maria magmatism was active, around ~4-3 Ga ago [3-5].
Recently, with the help of high resolution images a number of geologically young tectonic structures have been identified by various workers. Observations of small lunar graben depths and their crater crosscutting relationships indicate recent (<50 Ma) extensional tectonism [6]. Investigations of, contractional lunar lobate scarps using stratigraphy and crater size frequency distribution (CSFD) measurements has also shown that they are between 1 Ga to <100 Ma old [7,8]. In our work, we analyze several lunar wrinkle ridge systems in various lunar maria. Stratigraphic relationships and the lack of large superimposing craters suggests that wrinkle ridges in our study regions are Copernican, i.e. <1.1 Ga in age. For selected wrinkle ridge surfaces we derive model ages (AMAs) from CSFD measurements which result in ages below 30 Ma. Analyzed lunar wrinkle ridges appear morphologically crisp and include various degrees of pristine rocky outcrops. This suggests that they are geologically young because estimates of lunar boulder obliteration rates imply that rock populations on the lunar surface are fully destroyed in ~300-1500 Ma [9-12].

2. Methods and Data

In this work for CSFD measurements and stratigraphic analysis we use the Lunar Reconnaissance Orbiter Narrow Angle Camera (LRO NAC) dataset. Dating by the CSFD measurement technique has been previously used by various studies for small scale structures on the Moon such as lobate scarps, Irregular Mare patches (IMPs), impact ejecta and basalt flows [8,12,13]. This procedure relies on well-established lunar chronology and production functions [15,16]. For the identification of high concentrations of lunar boulders we use LRO Diviner instrument rock abundance maps derived from night and day time thermal infrared temperatures [17].

3. Results

All of the analyzed wrinkle locations across the Moon are shown in Fig. 1. Selected areas for CSFD analysis have exhibited very low crater frequencies. This lack of craters results in low derived absolute model ages (AMAs) from our CSFD measurements, all <30 Ma in age. One example wrinkle ridge cumulative CSFD plot can be seen in Fig. 2. All wrinkle ridges contain from low to high rocks abundancies. One wrinkle ridge system exhibits particularly high boulder concentrations in northern Mare Humorum, which is ~100 km in length, contains up to 5 different braids and has high thermal

Figure 1. Global view of analyzed wrinkle ridge locations. Larger circle area can be seen in Fig. 3. LRO WAC 100 m/px base map.

inertia values. The high reflective properties of these up to 5 meter boulders can be seen in Fig. 3.

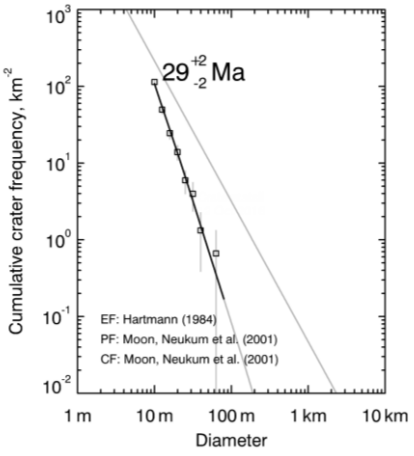

Figure 2. Cumulative CSFD plot and its model age for wrinkle ridge count area in Mare Imbrium.

4. Discussion and Conclusions

Our results suggest that there is some correlation between rocky terrains and low crater densities for wrinkle ridge areas analyzed in this work. The northern part of Mare Humorum (Fig. 3) according to standard dating techniques is 3.45 Ga of age [5]. The other mare regions exhibit similar old ages. The low model ages from CSFD measurements and the extremely rocky regions in Mare Humorum as well as other areas suggest of late Copernican (<100 Ma) global tectonic processes in the lunar maria. A recent study [18] has shown that along wrinkle ridges there are global stress fields. The processes that could excavate such amounts of lunar regolith and reshape the top layer of lunar maria is unknown. However, past Apollo missions have recorded deep and shallow lunar quakes [19,20]. The findings presented in this work and by other workers [7,8] point to a more complex lunar thermal and late stage tectonic evolution.

References

[1] Sharpton, V. L. and Head, J. W. *Proc. Lunar Planet. Sci. Conf.*, 307–317, 1988. [2] Plescia, J. B. and Golombek, M. P. 1986. *Geological Society of America Bulletin*, 97, 1289. [3] Basaltic Volcanism Study Project, *Basaltic volcanism on the terrestrial planets*, 1981. Pergamon Press, pp. 948–974. [4] Schultz, P. H. and Spudis, P. D. *Nature*, 302, 233–236, 1983. [5] Hiesinger, H. et al., *Geological Society of America Special Papers*, 477, 1-51, 2011. [6] Watters, T.R. et al., *Nature Geosci*, 2012. [7] Watters, T.R. et al., *Science*, 936-940, 2010. [8] Clark, J.D. et al. *LPSC XLVI*, 2015, Abstract #1730. [9] Basilevsky, A. T., et al. *Planetary and Space Science*, 89, 118-126, 2013. [10] Ghent R. R., et al., *Geology*, *42* (12), 1059-1062, 2014. [11] Basilevsky, A. T., et al. *Planetary and Space Science* 117, 312-328, 2015. [12] Ghent R. R., et al. *ELS 2016*, Abstract #6040. [13] Braden S. E. et al. *Nature Ge-osci.*, *7*, 2014. [14] Hiesinger, H. et al. *JGR*, 117, E00H10, 2012. [15] Neukum, G. et al. *Space Sci. Rev.*, 96, 55, 2001. [16] Neukum, G. *Meteoritenbombardement und Datierung planetarer Oberflächen*, Habil. Thesis, Univ. Munich, 1983. [17] Bandfield et al., JGR, E00H02, 2011. [18] Yue, Z. et al., *J. Geophys. Res. Planets*, 120, 978-994, 2015. [19] Nakamura, Y., *Proc. Lunar Planet. Sci. Conf.*, 1847-1853, 1980. [20] Nakamura, Y., *Physics of the Earth and Planetary Interiors*, 139, 197-205, 2003.

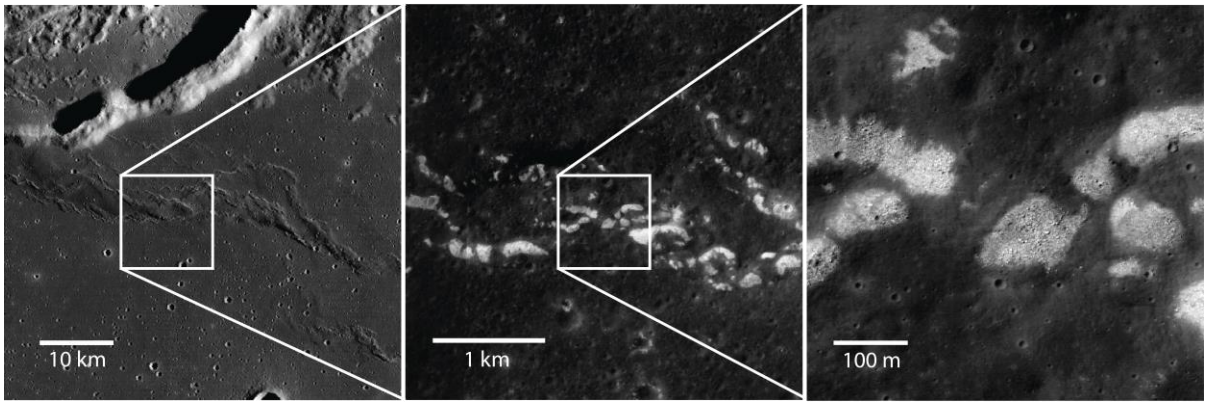

Figure 3. Context image of wrinkle ridge system in Mare Humorum (left). Close up images of rocky outcrops (center & right). LRO WAC and NAC (M183781901) images respectively. NAC low incidence angle image shown to emphasize the contrast between surrounding regolith and rocky outcrops.

EPSC Abstracts
Vol. 11, EPSC2017-968, 2017
European Planetary Science Congress 2017

The Spatial Extent of Lunar Impact Flashes

M. D. Menzies (1), **A. C. Cook** (1), S. Sposetti (2), R. Lena (3) and M. Iten (4)
(1) Aberystwyth University, UK (atc@aber.ac.uk), (2) Gnosca Observatory, Switzerland, (3) Geological Research Group (GLR) and BAA Lunar Section, Milan, Italy, (4) Garden Observatory, Switzerland.

Abstract

On the 1st January 2017, a small sub-kilogram mass meteoroid impacted into the Mare Nubium. The flash was observed independently from Switzerland and the UK. There are indications that the shape of this flash may not have been a point source, and we discuss terrestrial and lunar explanations for the cause of this.

1. Introduction

If a meteor strikes the Moon outside of a known meteor shower, then very little can be determined by terrestrial telescopic observations of the impact, other than its kinetic energy [1]. However, for three simultaneously observed lunar impact flashes, all on different dates, these suggest that there may occasionally be elongations to be seen in the flashes. If this effect were to be lunar in origin then this might help us to ascertain the impact azimuth, and whether this was related to a shallow incidence impacts. This could help narrow down candidate asteroidal or cometary orbit sources for the meteoroid, hence allow us to infer a velocity and estimate a mass.

2. 1st January 2017 Flash

On this date at 17:47 UT Stefano Sposetti (Gnosca) videoed and discovered a candidate lunar impact flash. Video from a remotely operated telescope at Aberystwyth University (UK) was later examined and confirmed the flash at a location of ~17.2˚ W, ~22.0˚ S, a few km to the NW of Wolf crater. An enlargement of both recorded flashes can be seen in Fig 1, where the images have been affine transformed together, so that they have the same scale and orientation. The Swiss flash appears larger than the British flash as the camera used in the former covered a larger area of the Moon, and so the spatial image scale was ~3.4 km/pixel, compared to ~2.1 km/pixel in the UK. Nevertheless both flashes show similar alignment along the SW-NE direction, with a small portion of the flash occurring to the SW of the pixel of greatest intensity and a significant portion to the NE. During the beginning of January the Earth encountered the Quadrantids meteor shower, targeting the Moon from the North, however none of these could have reached so far south. A smaller Delta Cancrids meteor shower also occurred during January and targeted most of the Earth facing side of the Moon, however these would have been approaching from the W., but this was not the direction the flash lay in.

Figure 1: Enhanced images of the 1/1/2017 impact flash observed North-West of Wolf crater. Flash on the left observed from Gnosca, Switzerland. The flash on the right observed from Aberystwyth, UK. These images are from TV fields, namely 1/50th and 1/60th sec respectively in duration.

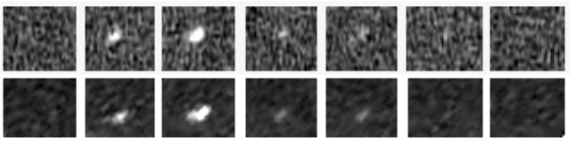

Figure 2: Time sequence of 1/60th sec TV fields of the 19/11/2001 UT 00:18:58 Leonid lunar impact flash (6˚ E, 15˚N), after alignment. (Top) from Alexandria, VA, USA, (Bottom) from White Rock, NM, USA.

3. 19th November 2001 Flash

On this date Anthony Cook (Alexandria, VA, USA) and David Palmer (White Rock, NM, USA) simultaneously videoed a 5th magnitude [1] lunar impact flash, which was assumed to be a lunar Leonid. Despite being approximately separated by 2.5 thousand km, the elongations of the flashes appear very similar, (see Fig 2). A third observer, David Durham, located near to the first observer,

recorded the flash too, however the image resolution and observing conditions were worse, and it showed no apparent elongation.

4. Other Non-Point Like Flashes

Images of a Perseid impact flash, taken on 12/8/2013 at 19:45:47 UT [2] (See Fig 4 from the referenced paper) reveal slight ellipticity. Furthermore an 8th magnitude candidate impact flash [3] from 26/2/2015, videoed by Marco Iten (Switzerland), located near Lippershey P, just on the dark side of the terminator, exhibited an apparent plume like effect spreading 80 km further onto the night side of the Moon and lasting several seconds.

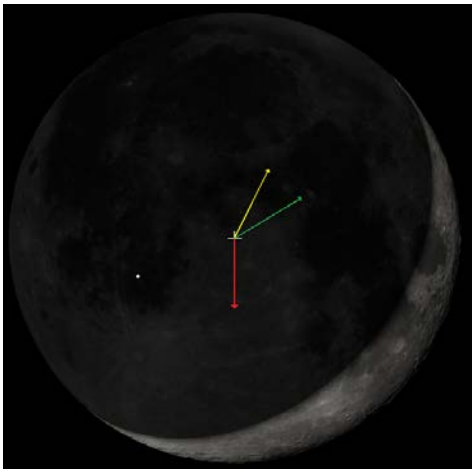

Figure 3: Computed generated phase and orientation of the Moon at the time of the Jan 1st 2017 impact flash from Aberystwyth. Red arrow represents direction to horizon. Yellow represents North on the Moon. Green represents apparent direction of the impact flash. White dot represents the impact site.

5. Discussion

Both the 2001 and 2017 flashes have elongations at significantly different angles to the perpendicular line of the Moon with respect to the observers' horizons, so this effectively rules out refractive effects [4] in our atmosphere as being a cause. Furthermore the impact flash observed simultaneously on 19/11/2001 showed similar morphology from both observing sites, as the flash developed (see Fig 2), which suggests that neither atmospheric turbulence, nor chromatic aberration in scope optics, can be a cause.

Hypothetically lunar topography could have an influence in the shapes of some flashes. For example, if a nearby mountain slope had been be illuminated by an especially bright flash on the lunar night side, this might alter the apparent spatial extent of the observed shape of the flash. Although the 19/11/2001 flash was on the western shore line of the Montes Appeninus, the impact on 1/1/2017 struck the Moon in a seemingly flat area of Mare Nubium.

Impact flashes near to the terminator could result in ejecta clouds being illuminated by sunlight, and may account for the 26/2/2015 event. However the other elongated flashes were all located far from the terminator.

We are uncertain as to a firm explanation of the effects we have seen, however we speculate that they may be a result of grazing or shallow angle impacts. This offers an explanation if the material from the meteoroid, and resulting ejecta, were thrown over kilometre scale distances. However this would necessitate the events seen on: 19/11/2001 and 12/8/2016, to be non-meteor shower impactors, unless the gradients of local meter scale topography, were steep enough to mimic shallow impacts angles?

We recommend that impact flash monitoring programmes attempt to record lunar impact flashes at a higher angular resolution, in future, to see if elongations, or spatial shapes in resulting fireballs, or ejecta clouds, are indeed detectable and confirmable. Greater than two simultaneous observations would help to eliminate any uncertainty.

Acknowledgements

Europlanet 2020 RI has received funding from the European Union's Horizon 2020 research and innovation programme under grant agreement No 654208 for the development of lunar impact flash detection software at Aberystwyth University. We would also like to thank David Palmer and David Durham for use of their images in our study.

References

[1] Cudnik. B., Lunar Meteoric Impacts and How to Observe Them, Springer, pp 240, 2010. **[2]** Madiedo, J.M. *et al., Astronomy and Astrophysics*, A118, p1-9, 2015. **[3]** Iten, M., *et al.*, *Selenology Today*, p. 4-11, March 2015. **[4]** Peach, D., Journal of the BAA, 122, p229, 2012.